Chandra Deep X-ray Observation of a Typical Galactic Plane Region and Near-Infrared Identification

K. Ebisawa[1,2,3], M. Tsujimoto[4], A. Paizis[2,5], K. Hamaguchi[1], A. Bamba[6], R. Cutri[7],
H. Kaneda[8], Y. Maeda[8], G. Sato[8], A. Senda[9], M. Ueno[9], S. Yamauchi[10], V. Beckmann[1],
T. J.-L. Courvoisier[2,11], P. Dubath[2,11], & E. Nishihara[12]

ebisawa@subaru.gsfc.nasa.gov

ABSTRACT

Using the *Chandra* Advanced CCD Imaging Spectrometer Imaging array (ACIS-I), we have carried out a deep hard X-ray observation of the Galactic plane region at $(l, b) \approx (28.°5, 0.°0)$, where no discrete X-ray source has been reported previously. We have detected 274 new point X-ray sources (4 σ confidence) as well as strong Galactic diffuse emission within two partially overlapping ACIS-I fields (~ 250 arcmin^2 in total). The point source sensitivity was $\sim 3 \times 10^{-15}$ ergs s^{-1} cm^{-2} in the hard X-ray band (2 – 10 keV) and $\sim 2 \times 10^{-16}$ ergs s^{-1} cm^{-2} in the soft band (0.5 – 2 keV). Sum of all the detected point source fluxes account for only ~ 10 % of the total X-ray fluxes in the field of view. In order to explain the total X-ray fluxes by a superposition of fainter point sources, an extremely rapid increase of the source population is required below our sensitivity limit, which is hardly reconciled with any source distribution in

[1] code 662, NASA/GSFC, Greenbelt, MD 20771

[2] INTEGRAL Science Data Centre, Chemin d'Écogia 16, 1290, Versoix, Switzerland

[3] Universities Space Research Association

[4] Department of Astronomy and Astrophysics, Pennsylvania State University, University Park, PA 16802

[5] IASF, Sezione de Milano, via Bassini 15, I-20133, Milano, Italy

[6] Cosmic Radiation Laboratory, RIKEN (The Institute of Physical and Chemical Research), 2-1, Hirosawa, Wako, Saitama 351-0198, Japan

[7] IPAC, California Institute of Technology, Mail Code 100-22, 770 South Wilson Avenue, Pasadena, CA 91125

[8] Institute of Space and Astronautical Science/JAXA, Yoshinodai, Sagamihara, Kanagawa, 229-8510 Japan

[9] Department of Physics, Kyoto University, Kitashirakawa Oiwake-cho, Sakyo-ku, Kyoto, 606-8502, Japan

[10] Faculty of Humanities and Social Sciences, Iwate University, Iwate, 020-8550, Japan

[11] Observatory of Geneva, 51 chemin des Maillettes, 1290 Sauverny, Switzerland

[12] Gunma Astronomical Observatory, 6860-86 Nakayama Takayama-mura Agatsuma-gun Gunma, 377-0702, Japan

the Galactic plane. Therefore, we conclude that X-ray emission from the Galactic plane has truly diffuse origin. Only 26 point sources were detected both in the soft and hard bands, indicating that there are two distinct classes of the X-ray sources distinguished by the spectral hardness ratio. Surface number density of the hard sources is only slightly higher than observed at the high Galactic latitude regions, strongly suggesting that majority of the hard X-ray sources are active galaxies seen through the Galactic plane. Following the *Chandra* observation, we have performed a near-infrared (NIR) survey with SOFI at ESO/NTT to identify these new X-ray sources. Since the Galactic plane is opaque in NIR, we did not see the background extragalactic sources in NIR. In fact, only 22 % of the hard sources had NIR counterparts which are most likely to be Galactic origin. Composite X-ray energy spectrum of those hard X-ray sources having NIR counterparts exhibits a narrow ~ 6.7 keV iron emission line, which is a signature of Galactic quiescent cataclysmic variables (CVs). We were able to carry out a precise spectral study of the Galactic diffuse X-ray emission without point source contamination, thanks to the superb *Chandra* spatial resolution. Confirming previous results, we have detected prominent emission lines from highly ionized heavy elements in the diffuse emission. In particular, the central energy of the iron emission line was determined as $6.52^{+0.08}_{-0.14}$ keV, which is significantly lower than what is expected from a plasma in thermal equilibrium. The downward shift of the iron line central energy may be explained either by a plasma in non-equilibrium ionization state, or hybrid of the 6.4 keV fluorescent line from non-thermal process and the 6.67 keV line from thermally equilibrium plasma.

Subject headings: Missions: *Chandra* – Galaxy: milky way - X-rays: Star: Galactic diffuse emission

1. INTRODUCTION

The Galactic X-ray source population has been studied from the very beginning of X-ray astronomy. The *Uhuru* satellite detected 339 X-ray sources all over the sky brighter than $\sim 2\times 10^{-12}$ ergs s^{-1} cm^{-2} in 2 – 10 keV (Forman et al. 1978). Most bright X-ray sources are concentrated near the Galactic bulge or distributed along the Galactic plane, indicating their Galactic origin. A high sensitive X-ray observation with direct imaging was made for the first time with the *Einstein* satellite (Hertz and Grindlay 1984) in the soft X-rays below ~ 4 keV. The *ROSAT* Galactic Plane Survey (Motch et al. 1991) was made as a part of the *ROSAT* all sky survey, but the energy range was again limited to below ~ 2 keV. These soft X-ray surveys were not able to penetrate the Galactic heavy absorption ($N_H \approx 10^{23}$ cm^{-2}), hence did not allow us to observe those X-ray sources located deepest in the Galactic plane or behind.

In order to observe completely through the Galactic plane and to determine the Galactic

source population, hard X-ray ($\gtrsim$ 2 keV) observation is indispensable. This was made possible with *ASCA*, the first imaging satellite in the hard X-ray energy band (Tanaka, Inoue, & Holt 1994). *ASCA* carried out systematic surveys on the Galactic plane (Sugizaki et al. 2001) and the center region (Sakano et al. 2002) down to the sensitivity limit $\sim 3 \times 10^{-13}$ ergs s^{-1} cm^{-2} in 2 – 10 keV. *ASCA*'s point source sensitivity was limited by source confusion due to its moderate X-ray mirror point spread function ($\sim 1'$). *ASCA* discovered more than two hundreds new X-ray sources on the Galactic plane region within the longitudes of $|l| \leq 45°$ (Yamauchi et al. 2002; Ebisawa et al. 2003). Many of them are heavily absorbed and not detected in soft X-ray bands. ASCA suggested an intriguing possibility that there may be still more dimmer, undetected hard X-ray sources in the Galactic plane. *How many Galactic hard X-ray sources are there in the Galactic plane? What are the origins of those dimmest Galactic hard X-ray sources?* Using *Chandra*, the most sensitive hard X-ray telescope in the history, we want to answer to these fundamental questions.

Besides the discrete Galactic X-ray sources, the Galactic plane itself has been known to emit hard X-rays (e.g., Worrall et al. 1982; Warwick et al. 1985; Koyama et al. 1986). The emission forms a narrow continuous Galactic ridge, thus it is called the Galactic Ridge X-ray Emission (GRXE). GRXE exhibits emission lines from highly ionized heavy elements such as Si, S and Fe, which suggests that GRXE originates in thin hot plasmas with a temperature of several keV (Koyama et al. 1986; Yamauchi and Koyama 1993; Kaneda et al. 1997). Whether GRXE is composed of numerous point sources or truly diffuse emission has been a big problem for a long time. *ASCA* was expected to answer this crucial question, but it was not powerful enough to separate numerous dim point sources and diffuse emission (Yamauchi et al. 1996; Kaneda et al. 1997; Sugizaki et al. 2001). The origin of GRXE remained unresolved with *ASCA*.

Chandra is an ideal satellite that is able to resolve GRXE into point sources with a superb spatial resolution of $\sim 0.''6$ (Weisskopf et al. 2002). For this purpose, using the *Chandra* Advanced CCD Imaging Spectrometer Imaging array (ACIS-I), we have carried out a deep hard X-ray observation of the Galactic plane region at $(l, b) \approx (28.°5, 0.°0)$, where extensive observation had already been made but no discrete X-ray source detected with *ASCA*. Our first result was presented in Ebisawa et al. (2001); we have found that only $\sim$ 10 % of the hard X-ray flux (2 – 10 keV) in the *Chandra* field is explained by the point sources brighter than $\sim 3 \times 10^{-15}$ ergs s^{-1} cm^{-2}. Also, by comparing the observed source number density with those measured at high Galactic regions, we have concluded that most of these hard X-ray point sources on the Galactic plane are background AGNs. Therefore, GRXE is truly diffuse emission.

We have made two slightly overlapping *Chandra* deep observations for our project, only the first of which was analyzed in Ebisawa et al. (2001). In Ueno et al. (2003), using both observations, we have made detailed spatial and spectral study of the peculiar supernova remnant candidate AX J1843.8-0352 in the field. In this paper, we will present full analysis of our two *Chandra* observations. The purpose of this paper is two-fold; (1) to study nature of the dimmest X-ray point sources in more detail with an aid of the near-infrared (NIR) follow-up observation using the New Technology Telescope (NTT) at the European Southern Observation (ESO), and (2) to investigate

for the origin of the Galactic diffuse emission through precise spectral analysis completely free from the contamination of point sources. Clean separation of the diffuse emission and point sources is great gift of the superb *Chandra* spatial resolution.

2. OBSERVATION AND DATA REDUCTION

2.1. X-ray Observation and Data Reduction

We observed the "empty" Galactic plane region at around $(l, b) \approx (+28°.5, 0°.0)$ in order to study the Galactic diffuse X-ray emission and dim point X-ray sources. This direction is toward the Scutum arm and is known to have strong diffuse emission, thus already extensively observed with *ASCA* (Yamauchi et al. 1996; Kaneda et al. 1997). *ASCA* did not detect any point source brighter than $\sim 2 \times 10^{-13}$ ergs s^{-1} cm^{-2} (2 – 10 keV), while it found an intriguing hard X-ray diffuse feature (AX J1843.8–0352; Bamba et al. 2001), which was another motivation for our *Chandra* observation in this region. We carried out each 100 ksec pointing on February 25, 2000 (AO1) and May 20, 2001 (AO2), respectively, with slightly overlapping fields. The total area of the observed field is ~ 250 arcmin^2.

In this paper, we have used the event data processed by the *Chandra* X-ray Center with the latest processing system in early 2003. Furthermore, we have applied position and energy calibration (CTI correction) using the CIAO package (version 3.0.1). The Two Micron All Sky Survey (2MASS)[13] was adopted for the position reference for *Chandra* as well as NTT/SOFI data (see the next subsection). Using the positions of those *Chandra* sources that have obvious NIR counterparts, we estimate our *Chandra* position accuracy as $\sim 0.''6$ (see also Section 3.4). Often the *Chandra* position accuracy is dominated by statistical error, in particular for the sources off-axis.

2.2. X-ray Point Source Extraction

First, we made exposure and vignetting corrected images in 0.5 –2 keV, 2 – 4 keV and 4 – 8 keV, and superposed them by assigning red, green and blue color respectively, followed by adaptive smoothing to enhance visibility (Fig. 1). We can clearly see many point sources as well as strong diffuse emission. We carried out point source search using the "wavdetect" program in the CIAO data analysis package. We searched for sources in the 0.5 – 3 keV (soft band), 3 – 8 keV (hard band) and 0.5 – 8 keV (total band) independently. We did not use data below 0.5 keV and above 8 keV in order to avoid high background in both energy ends. Sources that exceed 4 σ significance in any of the three energy bands were considered to be true detections. On the AO1 and AO2 overlapping field, we searched for the sources in the AO1 and AO2 data separately, and combined

---

[13]http://www.ipac.caltech.edu/2mass

the two significances quadratically if detected in both observations. We have detected 274 point sources within the total field of view. Source position and significance in each energy band, as well as distinction of AO1 or AO2, are given in Table 1. Position errors are the statistical ones calculated by wavdetect, not including any systematic errors.

None of these point sources has been reported in X-rays before. In the soft band, 182 sources have been detected, while in the hard band 79 sources. Only 26 sources are detected both in the soft and hard bands, suggesting an intriguing dichotomy in the source population (see Sections 3.3 and 3.4 for more details). Our sensitivity corresponds to $\sim 3 \times 10^{-15}$ ergs s^{-1} cm^{-2} (2 – 10 keV) and $\sim 2 \times 10^{-16}$ ergs s^{-1} cm^{-2} (0.5 – 2 keV). A new acronym "CXOGPE" (Galactic Plane sources reported by Ebisawa et al. 2004) is registered at CDS for the sources in Table 1 (See http://vizier.u-strasbg.fr/viz-bin/DicForm for detail). Hence, the first source in Table 1 at (18:42:51.77, $-3°51'11.''2$) may be formally designated as "CXOGPE J184251.7$-$035111", and so on. In this paper, however, the sources in Table 1 are referred as Source 1, 2, etc. for simplicity.

Sources 208, 210, 213, and 216, detected at around (R.A., Decl.)= $(18 : 43 : 57, -3°54'48'')$ seem to be parts of a single extended feature, which is designated as CXOU J184357-035441 by Ueno et al. (2003). This extended feature has a characteristic thermal spectrum (Ueno et al. 2003), and is probably a blob associated with the supernova remnant AX J 1843.8–0352/G28.6–0.1 (Bamba et al. 2001). All the other sources are consistent with the *Chandra* point spread function, thus they are considered as point sources.

2.3. NIR Observation and NTT/SOFI Data Reduction

Because of the heavy Galactic absorption, the NIR band has a great advantage over the optical waveband to identify dim X-ray sources on the Galactic plane. In fact, radio observation toward our field has been made (Dickey and Lockman 1990; Dame, Hartman and Thaddeus 2001; Minter et al. 2001), and the total hydrogen column density was estimated not less than $\sim 6 \times 10^{22}$ cm^{-2} (Ebisawa et al. 2001). This corresponds to $A_V \approx 33$ mag using the standard extinction formula ($N_H/A_V \approx 1.8 \times 10^{21}$ cm^{-2} mag^{-1}; Predehl and Schmitt 1995), so that there is hardly any hope to identify extragalactic sources or the most distant Galactic sources in the optical band. On the other hand, NIR extinction formulas $N_H/A_J \approx 5.6 \times 10^{21}$ cm^{-2} mag^{-1} (Vuong et al. 2003) and $N_H/E(J - K) \approx 10^{22}$ cm^{-2} mag^{-1} (Harjunpaeae and Mattila 1996) lead to $A_J \approx 11$ mag and $A_K \approx 5$ mag, hence NIR extinction is much smaller, and NIR observation will allow us to probe deeper into the Galactic plane.

The 2MASS database covers all the sky, and its Point Source Catalog gives the accurate positions and J, H and K_S magnitudes of all the major stars in our *Chandra* field of view (Fig. 2). In order to study more deeply than 2MASS, we have carried out a NIR follow-up observation at ESO using NTT (Tarenghi and Wilson 1989) with the SOFI infrared camera during the nights of 2002 July 28th and 29th. SOFI has 1024 × 1024 HgCdTe pixels with a moderately large field

of view ($4.'94 \times 4.'94$). The pixel size is $0.''2884$ pixel^{-1}, which is comparable to the *Chandra* one ($\sim 0.''5$ pixel^{-1}), thus very suitable to identify *Chandra* X-ray sources. We performed a mosaic observation composed of the 16 pointings slightly-overlapping each other to cover the central region of the two *Chandra* fields (Fig. 3). We defined seven central "A" fields and nine surrounding "B" fields to cover $\sim$ 75 % of the total *Chandra* field. The total exposure times for J, H and K_S bands for each A-field are 10, 10, and 14 minutes, respectively, and those for each B-field are 5, 5, and 7.47 minutes respectively. According to the standard SOFI observation procedure, we carried out a dithering observation, such that each field is covered by 5 (J and H band in B-field), 8 (K_S band in B-field), 10 (J and H band in A-field) or 15 (K_S band in A-field) sequential "frames", each jittered by $\sim 40''$. Exposure time for each frame was 60 (J and H bands) or 56 seconds (K_S band), and each frame was furthermore divided into 6 (J and H bands) or 8 (K_S band) read-out segments in order to avoid saturation. Thus, each frame was the average of the 6 (J and H bands) or 8 (K_S band) snap-shot images. The seeing was best in the first night ($\sim 0.''6$) when we observed fields A1 through A6 (only H and K_S bands for A6), whereas in the second night when we observed the remaining fields, the seeing was worse ($\sim 1.''5$).

IRAF[14] was mainly used to reduce the data following the standard procedure, i.e., subtraction of the dark current, flat-fielding using the dome flat, subtraction of sky using the median-sky technique, removal of bad pixels and cosmic-ray events, and trimming the frame edges. SExtractor (Bertin & Arnouts 1996) was used to extract sources. We searched for sources in each J, H and K_S band separately, and detected 16,890, 26,285 and 27,174 sources (with the DETECT_MINAREA, DETECT_THRESH, and ANALYSIS_THRESH parameter values 5, 1.5, and 1.5, respectively) in J, H and K_S bands, respectively. After removing the overlapping sources, 32,398 sources have been detected at least in one of the three bands (Table 2).

Using the 2MASS database as a reference, we have carried out astrometric correction and absolute magnitude calibration. In Fig. 4, we compare 2MASS and SOFI positions after the astrometric correction. The standard deviation of the shifts between 2MASS and SOFI is $0.''2$ in R.A. and Decl., which is smaller than the SOFI pixel size ($0.''2884$), and may be taken as a typical 2MASS and/or SOFI positional uncertainty. Considering the 2MASS source within $0.''2884$ radius as a counterpart, 8,655 SOFI sources are identified in 2MASS (Table 2).

In Fig. 5 we show correlation of the 2MASS and SOFI J, H and K_S magnitudes after the photometric correction. SOFI magnitudes tend to be larger than those of 2MASS for sources brighter than ~ 10 mag, where SOFI starts to saturate. Also, there is increasing confusion in the 2MASS-SOFI correlation for stars fainter than $J \approx 14$, $H \approx 13$ and $K_S \approx 12$, because of the relatively large 2MASS pixels. This leads to the increasing scatter in the 2MASS-SOFI photometric comparison. For the cleanest samples between 10 and 12 mag, the standard deviations of the 2MASS

– SOFI magnitude differences are 0.08, 0.10, and 0.12 mag in J, H, and K_S bands, respectively (for comparison, the 2MASS measurement precision for bright, non-saturated sources is $\sim$0.01 to 0.02 mags). These values may be considered as our typical photometric uncertainties.

Finally, in Fig. 6 we show cumulative histograms of the SOFI and 2MASS sources as a function of the SOFI magnitudes. We can see that our sample is almost complete down to $\sim$18, 17 or 16 mag in J, H, or K_S bands, respectively, if we assume extrapolation of the power-law source distribution at the brighter counts. The depletion of the sources dimmer than these limiting magnitudes may be due to our sensitivity limit and/or depletion of the intrinsic source population. We can also see the depth of our SOFI observation relative to 2MASS which saturates at around $\sim$16, 15 or 14 mag in J, H, or K_S bands, respectively.

3. DATA ANALYSIS AND RESULTS

3.1. Separation of the Diffuse Emission and Point Sources

One of the main purposes of the present observation is to cleanly separate the diffuse X-ray emission from the point sources, and to study the diffuse emission spectrum free from point source contamination. We have extracted an energy spectrum from both AO1 and AO2 data excluding the AX J 1843.8–0352/G28.6–0.1 region (marked in Fig. 1). Using the background database provided by *Chandra* X-ray Center (CXC), we have subtracted the background spectrum. The CXC background database is constructed from a set of blank sky observations at high Galactic latitudes excluding recognized celestial sources, thus it consists of particle background events and a small contribution from the dim extragalactic sources below the detection limit, as well as galactic or extragalactic diffuse emission at high Galactic latitudes (if any). Hence, after subtracting the background, our spectrum includes only point X-ray sources (Galactic and extragalactic) and Galactic plane diffuse emission, while uncertainty of the background subtraction may not be avoided (see also Section 3.6.2). In addition, we made an energy spectrum combining all the point sources in Table 1, subtracting the same background. In Fig. 7, we show the total energy spectrum and the combined point source spectrum, as well as difference between the two. We can see that only $\sim$ 10 % of the total X-ray emission in the *Chandra* field of view is explained by the sum of all the detected point sources. Even by extrapolating our $\log N - \log S$ curve downward, contribution of the point sources is rather minor (see Section 3.3). Therefore, the difference spectrum, explaining $\sim$ 90 % of the total flux, is considered to be mostly the Galactic diffuse emission (GRXE). We can see that emission lines from highly ionized heavy elements are associated with the diffuse emission. Although the presence of various emission lines in GRXE has been known for a long time (e.g., Koyama et al. 1986; Yamauchi and Koyama 1993; Kaneda et al. 1997), it is for the first time that the pure diffuse spectrum is extracted without point source contamination. More detailed diffuse emission spectral analysis is presented in Section 3.6.

3.2. Spectral Hardness-ratio and Source Fluxes

In order to study spectral characteristics of these new point sources, we computed energy flux and spectral hardness ratio (HR) for each source. The detected raw source counts do not represent the correct source intensities, since they are affected by positional dependence of the detector response (mostly mirror vignetting). Hence, we define and calculate the "normalized count rate" for each energy band, that is the count rate expected when the source is located on the ACIS-I aim point (on-axis direction) and observed for 100 ksec exposure. We define the spectral hardness ratio as $HR \equiv (H - S)/(H + S)$, where H is the normalized count rate in the hard energy band (3 – 8 keV), and S is that in the soft energy band (0.5 – 2 keV). The normalized count rates and HR are also shown in Table 1. Also, we plot the locations of the *Chandra* sources on the 2MASS image with different colors for soft, medium and hard sources (Fig. 2).

To determine source energy fluxes, we need to assume spectral models, but most sources are too dim to determine their energy spectra individually. Therefore, we took the following approach: first, energy spectra are extracted for all the sources (though most spectral bins have null counts), and corresponding instrumental responses were calculated. We categorized the sources into four spectral groups according to the hardness ratio; $HR < -0.8$, $-0.8 \leq HR < -0.2$, $-0.2 \leq HR < 0.6$ and $0.6 \leq HR$. For each spectral group, all the source spectra and responses were averaged. The background spectrum was extracted in the blank detector field for AO1 and AO2 separately, and subtracted from the average spectra after normalizing with the extraction area (thus, the Galactic diffuse emission is subtracted). Then, we fitted these four average spectra with an absorbed power-law model, and determined the average hydrogen column density and power-law index for each spectral group. Finally, each source in the same spectral group was "fitted" with the average spectral model only by adjusting the normalization. From the spectral model thus determined for each source, we calculated the 0.5 – 2 keV and 2 – 10 keV energy fluxes, which are shown in Table 1.

3.3. $\log N - \log S$ and Source Population

We study the point source number densities with the $\log N - \log S$ analysis in the hard band (2 – 10 keV) and soft band (0.5 – 2 keV) separately (Fig. 8). The $\log N - \log S$ curve in the hard band using only the AO1 data was already presented in Ebisawa et al. (2001). We take energy fluxes in Table 1, but our sample is not complete at the lowest flux ends. Therefore we set the lower flux limits at 3×10^{-15} ergs s^{-1} cm^{-2} in the hard band and 2×10^{-16} ergs s^{-1} cm^{-2} in the soft band, respectively, below which we do not discuss source populations. In Fig. 8, we also show the number of the hypothetical point sources below our sensitivity limit whose sum would account for the 100 % of the total X-ray fluxes observed in our field of view. We can clearly see that the actual observed source population is far below the number of point sources required to account for the total GRXE (see also discussion in Section 4.2).

We compare our Galactic plane $\log N - \log S$ curves with those of bright *ASCA* Galactic sources (Sugizaki et al. 2001), extragalactic point sources detected with *ASCA* (Ueda et al. 1999), *ROSAT* and *Chandra* (Giacconi et al. 2001). In addition, we have analyzed the *Chandra* Galactic center Sgr B2 region data (observed in 2000 March 29 for 100 ksec, obsID=944; Murakami, Koyama and Maeda 2001) in a similar manner to our Galactic plane data analysis, and made $\log N - \log S$ curves for both energy bands. The $\log N - \log S$ curves in the Sgr A region are also plotted (mathematical formulas taken from Muno et al. 2003). The extragalactic sources are significantly absorbed on the Galactic plane with a hydrogen column density of $N_H \approx 6 \times 10^{22}$ cm^{-2} (Section 2.3). Assuming a typical photon index of 1.7, we took into account the flux reduction due to the Galactic absorption, and made $\log N - \log S$ curves of the extragalactic sources expected to be seen through the Galactic plane (dashed lines in Fig. 8).

Let's compare our Galactic plane $\log N - \log S$ curves with those for extragalactic sources. In the soft energy band, number of the *Chandra* sources detected above the lowest flux limit is more than 20 times higher than that expected from the extragalactic sources through the Galactic plane (dashed line). Therefore, it is no doubt that most of the soft sources are Galactic. On the other hand in the hard energy band, the situation is quite different; the extragalactic $\log N - \log S$ curve explains most of the observed sources on the Galactic plane. Hence, the observed dichotomy of the source population (Section 2.2) may be naturally explained in that most of the soft X-ray sources have the Galactic origin, while most hard X-ray sources are extragalactic.

Comparison of the source populations in the Galactic plane ($l \approx 28.^{\circ}5$), Sgr A ($l \approx 0^{\circ}$) and Sgr B2 ($l \approx 0^{\circ}.5$) is also interesting. In the hard energy band, the source number density increases dramatically toward the Galactic center, significantly exceeding that on the Galactic plane and extragalactic one. This indicates that there are much more Galactic point sources in the Galactic center region than in the Galactic plane. In the soft band, on the other hand, the source number density at the lowest flux level is not so different on the Galactic plane and at the Galactic center regions. This is probably because the faintest observable soft sources are mostly located in our neighborhood, so that the direction toward the Galactic center or Galactic plane will not make a big difference. In fact, such dim soft sources at the Galactic *center* will be more significantly absorbed ($N_H \approx 10^{23}$ cm^{-2}) than those *extragalactic* sources in our Galactic *plane* field ($N_H \approx 6 \times 10^{22}$ cm^{-2}) , and are thus hardly detected.

3.4. NIR Identification and Source Classification

We may classify the new X-ray sources according to the HR. We define the "soft" sources whose HR are equal or less than the median $HR = -0.60$. For the rest, the median is $HR = 0.11$, so the "medium" and the "hard" sources are defined as those with $-0.59 < HR \leq 0.10$ and $0.1 < HR$, respectively. Excluding the sources obviously associated to an extended structure, number of the soft, medium and hard sources we have detected is 136, 65 and 69, respectively (Table 3).

Our *Chandra* position accuracy is mostly limited by photon statistics and distortion of the point spread function. We may expect an error of $\sim 1''$ for dim sources far from the aim points. We consider the NIR sources found within $\sim 1''$ of the *Chandra* positions as counterparts. For the *Chandra* sources in the SOFI fields (~ 75 % of all the *Chandra* sources; Table 3), we show SOFI counterparts in Table 1. 2MASS counterparts are given in Table 1 for the *Chandra* sources outside of the SOFI fields.

In Fig. 9, for each of the *Chandra* sources in the SOFI fields, we plot the relative positional difference to the nearest SOFI source. It is easily seen that most of the soft sources have the NIR counterparts, while medium and hard sources are less likely to have counterparts. In fact, the percentage of the *Chandra* sources having the SOFI counterparts is 83, 53, and 22 % for soft, medium, and hard sources, respectively (Table 3). For all the *Chandra* sources, the percentage with 2MASS counterparts is 45, 26 and 12 %, respectively (Table 3). The fact that the detectability of the NIR counterparts decreases with HR is consistent with the conclusion in the previous section that most soft sources are Galactic, while most hard sources are extragalactic. In fact, if these hard X-ray sources are background AGNs, assuming a typical X-ray/NIR luminosity ratio and the significant Galactic extinction, they are too dim to be detected in the NIR band (see discussion in Section 4.1).

In Fig. 10 (top), we show histograms of the number of sources as a function of HR. It is curious to see that the softest sources are most numerous, and that the number of sources first decreases with HR till $HR \sim 0.5$ and then increases again. On the other hand, number of the sources having NIR counterparts decreases monotonically with increasing HR. This also suggests that our source population is composed of the numerous Galactic soft sources and the less numerous extragalactic hard sources.

The bottom panel of Fig. 10 shows the normalized X-ray counting rates (Section 3.2) versus HR, as well as the presence or absence of the NIR counterpart for each source. We see that almost all the soft sources have NIR counterparts, except several of the dimmest ones. On the other hand for the hard sources, the presence or absence of the NIR counterparts is not related to the X-ray brightness. These facts are also seen in the $\log N - \log S$ curves (Fig. 8) made only from the X-ray sources identified with NIR (either by SOFI or 2MASS). These results suggest that hard X-ray sources without NIR counterparts are mostly extragalactic AGN whose X-ray intensities are widely distributed. In fact, the brightest hard source (Source 200) is not identified in NIR, thus considered to be a strong AGN candidate. Most bright soft X-ray sources are presumably nearby stars and thus they are identified in NIR. On the other hand, those unidentified soft X-ray sources are presumably intrinsically dim in NIR compared to soft X-ray fluxes (see discussion in Section 3.5.2). A small number of the hard sources with NIR counterpart are considered to be Galactic CVs, as we shall see below from detailed X-ray (Section 3.5.2) and NIR analysis (Section 4.1).

3.5. X-ray Characteristics of the Point Sources

3.5.1. X-ray Spectra/Hardness

Since most X-ray sources are too dim (as low as ~ 10 counts) to make individual spectra, we combined the sources having similar spectral hardness and made average energy spectra to investigate the spectral characteristics as a class. We categorized all the point sources into six groups, three ranges of the X-ray spectral hardness (Section 3.4), and further grouped according to the presence or absence of the NIR counterparts. We made an averaged energy spectrum for each group.

In Table 4, we show the spectral parameters of the six spectra fitted with a simple absorbed power-law model. When the number of sources combined is small, the power-law photon-index is not constrained tightly. In such cases, for a given spectral hardness, the photon index was determined from the group having more sources, either with or without NIR counterpart, and fixed for the other group. This also helps to clarify the difference of the hydrogen column densities and normalizations between the two groups. Since the hydrogen column density is a measure of the distance to the sources, this suggests that the medium and the hard sources are more likely to be located further than the soft sources. Also, the medium and hard sources without NIR counterparts show clear excess of the hydrogen column densities compared to those with the counterparts, which implies that the medium and hard sources without the counterparts tend to locate further (primarily extragalactic), than those with the counterparts which are more likely to be Galactic. On the other hand, if we compare the soft sources with NIR counterpart and those without counterpart, the average X-ray energy flux of the formers is $\sim 40\ \%$ smaller than the latter. This suggests that the soft X-ray sources without NIR counterpart are further than and/or intrinsically dimmer than those with NIR counterpart. It is remarkable that the hydrogen column densities are almost the same for both groups of the soft sources, suggesting that the distance is not the main factor to distinguish the two groups. On the other hand, for medium and hard sources, those without the NIR counterparts are *brighter* in both the observed fluxes and the intrinsic fluxes (Table 4). This is considered that significant parts of the hard and medium sources without NIR counterparts are extragalactic, and that they are X-ray bright AGNs which cannot be seen in NIR. A small number of the hard sources having NIR counterpart is likely to be Galactic. Quiescent CVs are strong candidates for these faint Galactic hard X-ray sources (e.g., Mukai and Shiokawa 1993; Watson 1999). A schematic view of explaining the situation is shown in Fig. 11.

3.5.2. Spectral Fitting

In the previous section, we used a simple absorbed power-law model to study the difference of the six average spectra (Table 4). Here, we fit the average source spectra with more physically meaningful models, and also study the iron line feature more carefully.

The X-ray energy spectrum of an active stars is characterized by a two temperature plasma model. Therefore, we used a two temperature MEKAL model in XSPEC (version 11.3.1) for the soft spectrum with NIR counterparts. The spectrum is well fitted with a two temperature plasma at 0.2 keV and 2.0 keV (Table 5). An ionized iron emission line is expected from the high temperature plasma, and indeed there is an evidence of iron emission line though not very strong (Fig. 12, top left). Assuming that the soft sources without NIR counterpart have the same X-ray spectral properties, we tried exactly the same spectral model (including N_H) and allowed only the overall normalization to be a free parameter. We found the fit is reasonably well, with 52 % of the normalization of the soft sources with NIR counterpart (Fig. 12, top right). As we shall see later (Section 4.1; Fig. 19 top), there is a general trend of correlation between NIR fluxes and soft X-rays, primarily accounted for by the distance, while NIR fluxes show large intrinsic scattering (several magnitudes) for a given soft X-ray flux. Reduction of the flux to 52 % corresponds to only ~ 0.7 mag change, which does not explain the non-detection in NIR. Therefore, we conclude that those soft X-ray sources without NIR counterpart are intrinsically dim in NIR relative to the soft X-ray luminosity.

Average energy spectrum of the hard sources with NIR counterparts exhibits a conspicuous narrow iron emission line (Fig. 12, bottom left). The line center energy is 6.67 keV and the equivalent width is 540 eV (Table 5), which is expected in thermal emission from faint CVs (e.g., Ezuka and Ishida 1999). These iron line parameters and the flat spectrum (photon-index = 1.47) correspond to a plasma temperature of $kT \sim 8$ keV. On the other hand, the hard sources without NIR counterparts do not show a narrow iron emission line, but have a broad line and an edge feature which may be modeled with a neutral iron edge (at 7.11 keV) and a broad emission line (at 6.67 keV, EW = 340 eV). These iron features as well as the flat spectrum (photon-index = 0.77) are reminiscent of the disk reflection spectrum often seen in Type II AGN.

The average spectrum of medium sources with NIR counterpart can be fitted with two temperature plasma model, in which the soft component temperature (0.2 keV) is similar to that of the soft spectrum but the hard component temperature is higher (2.9 keV), suggesting a mixture of the relatively hot stars and soft CVs. The average spectrum of medium source without NIR counterpart can be fitted with a power-law which is steeper and less absorbed than the hard sources, presumably indicating a composite of faint hot stars and soft AGNs.

3.5.3. Time Variation

We study time variation of the point sources. For each source, we have made two light curves with bin-widths of 3,000 sec and 10,000 sec. We performed the Kolmogorov-Smirnov test, and if both light curves show variations above 99.9 % significance level, we consider the source to be significantly variable. In our sample, 17 sources are found to be variable, which are marked in Table 1 ("T" in the first column). The distribution of the hardness ratio for these variable sources is shown in Fig. 10 (blue circles). We may not find a clear correlation between the spectral hardness

and source variability, besides that there are no variable sources harder than $HR = 0.43$. This might imply that in our sample the soft Galactic sources are more variable than the hard AGNs, but this is not conclusive being limited by the number statistics. Besides, several soft sources exhibit characteristic flare-like variations, such as rapid rise and/or exponential decay, as shown in Fig. 13. The average HR is -0.51 for these seven sources. The flare-like activity and spectral softness are considered to be a signature for the X-ray active flare stars.

3.6. Spectral Study of the Diffuse X-ray Emission

3.6.1. Line Emission

At first, we concentrate on the iron and other emission lines. We fit the iron energy band (5.5 – 7.2 keV) and soft energy band (0.8 – 3.5 keV) separately with a simple power-law plus gaussian model, and determine the line parameters.

We point out that ACIS-I iron line measurement has a significant merit in that contaminating instrumental iron line, which was problematic in *ASCA* and *XMM-Newton* diffuse spectral study, is almost fully negligible. In the iron energy band, a single narrow gaussian model is successful (Table 6; Fig. 14, top). The central line energy is $6.52^{+0.08}_{-0.14}$ keV (90 % error), which is consistent with Kaneda et al. (1997; 6.61 ± 0.02 keV), and significantly lower than what expected from He-like iron in a thermally equilibrium plasma (6.67 keV). A possible explanation of the line energy shift is that the plasma is in non-equilibrium ionization (NEI) state (Yamauchi and Koyama 1993; Kaneda et al. 1997), or the line is composed of a fluorescent 6.4 keV line and a thermal 6.67 keV line (Valinia et al. 2000b). Considering the latter possibility, we fit the same spectrum with a multiple line model. In addition to these two lines, if the charge exchange takes place between the cosmic-ray iron nuclei and interstellar hydrogen atoms (Tanaka, Miyaji, & Hasinger 1999; Tanaka 2002), a hydrogenic iron line at 6.97 keV is expected. Thus, we fit the observed spectrum with the three lines with fixed energies (Table 6; Fig. 14, bottom). The fit is acceptable, though slightly worse than with the single line model. The cosmic-ray charge exchange model predicts significantly broadened emission lines due to the energetic cosmic-ray bulk motion (Tanaka, Miyaji, & Hasinger 1999; Tanaka 2002), but from our statistics we could not constrain the intrinsic iron line width.

We point out that the iron line equivalent width in GRXE is significantly dependent on the spectral model, and difficult to be determined uniquely both in *Chandra* and *ASCA* observations. With a single narrow line model we obtained $EW = 170 \pm 120$ eV, which is smaller than the *ASCA* value with the same model and same sky region, 405 ± 80 eV (Kaneda et al. 1997). Contamination of the point sources with strong iron emission in the *ASCA* spectrum might explain the different at least to some extent. On the other hand, with the three line model, our equivalent width values are 100^{+50}_{-100} eV, 180^{+360}_{-140}, and 160^{+260}_{-160} eV, which are consistent with the *ASCA* result using the same three line model on the same sky, < 70 eV, 280 ± 70 and 120 ± 70 eV (Tanaka 2002), though errors are large.

Similarly, the soft band energy spectrum was fitted with a power-law continuum and eleven gaussians (Table 7; Fig. 15). These are the same lines detected in *ASCA* (Kaneda et al. 1997), with the additional Si XIII $K\beta$ line at at 2.18 keV. Equivalent width values are consistent with those in Table 4 in Kaneda et al. (1997), except that we find much weaker 1.74 keV (low ionized Si) and 2.00 keV (Si XIV,Lyα) lines.

3.6.2. Fit with Non-Equilibrium Ionization Plasma Model

We now try to fit the observed diffuse spectrum with a more physically reasonable model. As a working hypothesis, we adopt the same spectral model used by Kaneda et al. (1997), which is a two temperature NEI model (Masai 1984), such that there are soft and hard NEI components which have different temperatures, normalizations, ionization parameters and are affected by different amounts of interstellar absorption.

First, we fix the element abundances for the soft component and hard component, respectively (Table 8 left; Fig. 16 top). The fit is not satisfactory (reduced $\chi^2 = 1.97$), and in particular, the observed iron and neon emission lines are not explained. Next, we adjust abundances of Ne, Mg, and Si in the soft component, and Fe abundance in the hard component (Table 8 right; Fig. 16 bottom). Now the fit is better (reduced $\chi^2 = 1.52$), though artificial adjustment of the abundances is unexplained. Still, we notice a hint of high energy excess above iron line energy, which may be related to the non-thermal component reported above ~ 10 keV (Yamasaki et al. 1997; Valinia et al. 2000b), though this range of the spectrum is subject to the background uncertainty.

With the two component model fit, we have determined the observed flux from the soft and hard component as 2.6×10^{-8} and 2.1×10^{-7} ergs cm^{-2} s^{-1} str^{-1} (0.7 – 10 keV), respectively. If the absorption is removed, the intrinsic fluxes are 1.1×10^{-7} and 7.6×10^{-7} ergs cm^{-2} s^{-1} str^{-1} (0.7 – 10 keV), respectively. Note that the observed flux and spectral shape are significantly affected by the heavy interstellar absorption (Fig. 17). Although the soft component is dominant in the observed flux below 2 keV, the hard component is more dominant over the entire energy band if absorption is removed. Using the same two component model, Kaneda et al. (1997) gave the intrinsic (= absorption removed) soft and hard component fluxes 1.9×10^{-6} and 5.3×10^{-7} ergs cm^{-2} s^{-1} str^{-1} (0.5 – 10 keV), respectively. We remark that, in the NEI models we assume, strong oxygen lines are expected between 0.5 keV and 0.7 keV (Fig. 17), which are hardly observable below the low energy thresholds of both *ASCA* and *Chandra*. Therefore, it will be more reasonable to compare the fluxes in 0.7 – 10 keV, not in 0.5 – 10 keV. Calculated from the NEI model parameters by Kaneda et al. (1997), the observed soft and hard component fluxes with *ASCA* are 5.3×10^{-8} and 1.2×10^{-7} ergs cm^{-2} s^{-1} str^{-1} (0.7 – 10 keV), respectively, and the intrinsic soft and hard component fluxes are 1.9×10^{-7} and 4.3×10^{-7} ergs cm^{-2} s^{-1} str^{-1} (0.7 – 10 keV), respectively. Compared to the *ASCA* result, the *Chandra* flux in 0.7 – 10 keV is ~ 40 % higher, while the soft component flux is ~ 50 % smaller and the hard flux is ~ 80 % higher. The difference is presumably caused by systematics such as slight difference of the sky, uncertainty of the background, and mirror

responses, etc. For example, we have subtracted the background taken at high Galactic latitudes, which might include soft photons from AGNs below detection threshold. Also, local soft diffuse emission surrounding the solar system is presumably higher at high Galactic latitudes. Since these photons are completely absorbed in our Galactic plane field, we may have over-subtracted soft X-ray background, which might explain the smaller soft component flux compared to *ASCA*. In any case, our *Chandra* GRXE measurement is considered to be most precise in the sense that it is free from the point source and stray-light contamination which significantly affected the *ASCA* GRXE measurement.

4. Discussion

4.1. Origin of the Point Sources

We have detected 270 point X-ray sources (above 4 σ significance) on a typical Galactic plane field at around $(l, b) \approx (28.°5, 0.°0)$ within ~250 arcmin^2, down to the flux limits $\sim 3 \times 10^{-15}$ erg s^{-1} cm^{-2} (2 – 10 keV) or $\sim 2 \times 10^{-16}$ erg s^{-1} cm^{-2} (0.5 – 2 keV). Thus, we were able to extend the Galactic X-ray source $\log N - \log S$ curves to much dimmer levels compared to the previous observations. In the brightest end, our $\log N - \log S$ curves match well with those made by *XMM-Newton* (Hands et al. 2004) and *ASCA* (Sugizaki et al. 2001) on much larger Galactic plane region.

Based on the X-ray spectral properties and presence or absence of the NIR counterparts, we have presented a schematic view of the origin of point X-ray sources (Fig. 11). Namely, hard X-ray sources without NIR counterpart are extragalactic, those with counterpart are Galactic CVs, while soft X-ray sources are nearby active stars. For the hard sources without NIR counterpart, assuming the average X-ray flux (Table 4) a typical broad-band spectrum of AGN with photon-index of 2 (flat energy spectrum in the $\nu F\nu$ plot), we estimate the expected J, H and K_S magnitudes as 22.7, 22.0 and 21.1, respectively. Taking into account the further reddening $A_K \approx 5$ (Section 2.3), we see that there is almost no hope to detect those background AGNs through the Galactic plane. Even though the above estimate is wrong by a large factor, it is very difficult to see the background AGNs even using the most powerful telescopes. It appears much easier to detect them in hard X-rays.

To understand the properties of the point sources with NIR counterpart, we have made a NIR color-color diagram (Fig. 18). We can see that most soft X-ray sources are along the track of the heavily reddened main sequence stars, which, together with the thin thermal X-ray spectra (Fig. 12), strengthens the stellar origin of the soft X-ray sources. From the X-ray spectral similarities of the soft X-ray sources with and without NIR counterparts, we concluded that soft X-ray sources without NIR counterparts are also likely to be stars (Section 3.5.2). On the other hand, isolated neutron stars can be dim ($\sim 10^{-16}$ ergs cm^{-2} s^{-1}) soft X-ray sources without optical/NIR counterparts (Popov et al. 2000). Popov et al. (2000) estimated expected number of such isolated neutron stars

as one per square degree, namely, ~ 0.07 in our *Chandra* field. Therefore, there is hardly a chance that there is an isolated neutron star among our 38 soft X-ray sources without NIR counterparts. Isolated neutron stars should exhibit purely blackbody spectrum, so future high quality X-ray observations of individual sources will distinguish isolated neutron stars and active main sequence stars.

Furthermore, for the X-ray sources with NIR counterpart, we studied the correlation between the X-ray fluxes and the NIR magnitudes (Fig. 19), and correlation between the X-ray spectral hardness and the X-ray to NIR flux ratios (Fig. 20). From Fig. 18 to 20, we notice the following X-ray and NIR characteristics of the sources:

1. On the NIR color-color diagram, the medium and hard X-ray sources are more scattered than the soft X-ray sources that are mostly on the main-sequence track (Fig. 18).

2. Soft X-ray and NIR fluxes are correlated, and the correlation is along the slope expected for the constant luminosity sources at different distances (Fig. 19), though NIR flux variance is large for a given soft X-ray flux. On the other hand, the correlation is not clearly seen between hard X-rays and NIR fluxes.

3. The X-ray spectral hardness and the X-ray to NIR flux ratio show correlations, that is more significant in hard X-ray fluxes than in soft X-rays (Fig. 20).

The above facts (1) and (2) suggest that most soft X-ray sources are active stars, and that variance of both soft X-rays and NIR fluxes is primarily explained by difference of the distance. It is known that CVs are more scattered on the NIR color-color diagram than main sequence stars (Hoard et al. 2002) or AGNs (Cutri et al. 2005). In particular, the distribution of our hard X-ray sources on the NIR color-color diagram (Fig. 18) seems to be similar to that of "uncertain/unclassified" CVs in Hoard et al. (2002). The NIR study thus supports the idea that most of the Galactic hard X-ray sources in our sample are CVs, that is already suggested from X-ray spectral study (Section 4.1). The above fact (3) is presumably indicating intrinsic differences in the hard X-ray fluxes/NIR flux ratio of active stars and CVs, such that CVs are relatively bright hard X-ray sources compared to the NIR fluxes. The new hard X-ray sources we discovered with NIR counterpart have not been previously identified as CVs in optical or any other wavelength (e.g., Downes et al. 2001). Therefore, a hard X-ray observation may be an efficient mean to discover previously unknown or unclassified CVs. Vice versa, those unclassified CVs may be detected in hard X-rays, which may be experimented by *Chandra* and/or *XMM-Newton*.

4.2. Origin of the Galactic Diffuse X-ray emission

We have detected point sources brighter than 3×10^{-15} ergs s^{-1} cm^{-2} (2 – 10 keV) and 2×10^{-16} ergs s^{-1} cm^{-2} (0.5 – 2 keV), and excluded these point sources to study the Galactic diffuse emission

spectra. Using the best-fit model (Section 3.6), the observed diffuse emission flux is 6.5×10^{-11} ergs s^{-1} cm^{-2} deg^{-2} (2 – 10 keV) and 8.7×10^{-12} ergs s^{-1} cm^{-2} deg^{-2} (0.5 – 2 keV). Let's consider if this "diffuse" emission may be accounted for by superposition of the still dimmer point sources below our detection limits. In Fig. 8, we show numbers of the hypothetical point sources whose sum would account for 100 % of the Galactic ridge X-ray emission. These numbers are calculated by subtracting the contribution from the detected point sources from the total observed X-ray fluxes, then divided by a given point source flux below our detection limit. So that all the detected diffuse emission is explained by the point sources alone, it is required that the $\log N - \log S$ curves rapidly steepen by an order of magnitude below our sensitivity. No spatial distribution of point sources in the Galactic plane would accommodate such an unusual $\log N - \log S$ curve. Based on similar arguments, Muno et al. (2004) concludes that the Galactic center diffuse emission is either truly diffuse or accounted for by a completely new population of faint sources ($< 10^{31}$ ergs s^{-1}) that are at least 10 times more numerous than any known population. They reserved the point source possibility, because there might be such numerous and exotic sources inhabiting *locally* the Galactic center region that itself is a mystery. However, our observation is a typical Galactic region, and the source population should reflect the *global* X-ray source distribution through the Galactic plane. Hence, we may not expect unusual behavior of the Galactic $\log N - \log S$ curves such as a sudden steepening by an order of magnitude.

Considering the spectral similarity of the diffuse emission on the Galactic plane (Section 3.6) and Galactic center (Muno et al. 2004), we are tempted to conclude that they have similar origins (see also Tanaka 2002). Recent INTEGRAL observations have detected hard X-ray emission above 20 keV in the Galactic center region whose centroid is slightly offset of Sgr A* (Bélanger et al. 2004), but coincides with the center of the diffuse component imaged by *Chandra* (Muno et al. 2004). This suggests that a non-thermal hard-tail of the Galactic center diffuse spectrum is extended above 20 keV. GRXE also has a power-law hard-tail component which extends above ~20 keV (Yamasaki et al. 1997; Valinia and Marshall 1998). On the other hand, strong diffuse gamma-ray (~ 100 keV – 1 MeV) emission is observed from the Galactic center and plane region (e.g., Gehrels and Tueller 1993; Skibo et al. 1997; Valinia et al. 2000a; Strong et al. 2003), which is suggested to have a non-thermal origin, as the energy spectrum is represented with a power-law without a thermal cut-off. Intriguingly, the Galactic center and plane diffuse hard X-ray components seem to be smoothly connected to the gamma-ray components, although their physical relationship has not been understood.

We found that GRXE has a truly diffuse origin, then the question is how to produce and maintain such high energetic plasma. There are obvious problems in interpreting GRXE in terms of simple equilibrium thermal plasma, such that the plasma temperature needed to explain the observed spectra, $kT \approx 5 - 10$ keV, is much higher than can be bound by Galactic gravity (Warwick et al. 1985). Also, the energy density of GRXE, ~ 10 eV/cm^3, is one or two orders of magnitude higher than those of other constituents in the interstellar space, such as cosmic rays, Galactic magnetic fields, or ordinary interstellar medium (Koyama et al. 1986; Kaneda et al. 1997). Currently

there are no accepted theoretical models that can explain the origin of GRXE. Some argue that the interstellar magnetic field is playing a significant role to heat and confine the hot plasma (Tanuma et al. 1999). Others propose that the interstellar medium is mainly responsible for GRXE and gamma-ray emission, via interactions with, for instance, low energy cosmic-ray electrons (Valinia et al. 2000b), in situ accelerated quasi-thermal electrons (Dogiel et al. 2002; Masai et al. 2002), or heavy ions (Tanaka, Miyaji, & Hasinger 1999). Galactic particle acceleration is considered to take place in supernova remnants. Serendipitous discovery of the hard X-ray emitting supernova remnant AXJ 1843.8–0352 in our field (Bamba et al. 2001; Ueno et al. 2003) in fact strongly suggests a close tie between GRXE and supernova remnants.

Various theoretical models of GRXE have to be tested through observations. Different heating or acceleration mechanism of the plasma will result in different plasma conditions, which are reflected in the emission lines. Therefore, from precise measurements of the emission lines in GRXE, we may in principle diagnose the plasma conditions and constrain the theoretical models. In particular, iron line spectroscopy is essential. We have shown that the GRXE iron line central energy is $6.52\pm^{0.08}_{0.14}$ keV (Section 3.6), significantly lower than what expected from thermally equilibrium plasma ($\sim$6.67 keV). Although we could not distinguish if the iron line we detected is a single line or composite of two or three lines, a high signal-to-noise *Chandra* Galactic center diffuse spectrum clearly indicates the three emission lines from low ionized iron, He-like iron and H-like iron (Muno et al. 2004). If we assume similar origins of Galactic center and plane diffuse emission, then the three line interpretation of GRXE iron line emission seems plausible (see also Tanaka 2002). If this is the case, the 6.4 keV line is considered from fluorescence in cool interstellar medium, which may be induced, for instance, by low energy cosmic-ray electrons (Valinia et al. 2000b). Both He-like and H-like lines may be from, for example, the thermal equilibrium plasma, the charge exchange process of iron ions (Tanaka, Miyaji, & Hasinger 1999; Tanaka 2002), or the interaction between in-situ accelerated electrons and cool ($kT < 1$ keV) plasma (Masai et al. 2002). These cases may be distinguished from intrinsic line widths, since in the second case the lines are expected to be significantly broadened by the iron nucleus bulk motion (Tanaka et al. 2000), while on the other hand in the last case the lines are expected to be narrow since the plasma is cold.

We emphasize that the precise iron line diagnostic (including line intrinsic width measurement) is a key to resolve then origin of the Galactic center and Galactic plane diffuse emission. In this context, planned Galactic center observations with Astro-E2 XRS, the first X-ray microcalorimeter in space with $\sim$ 6 eV resolution, will be an enormous help. GRXE may be too dim for Astro-E2 XRS (our simulation suggests that a million second exposure is required), but we believe that the long standing mystery of GRXE will be certainly solved by the future calorimeter observations with higher throughputs and better spectral resolution, expected to be made by *Con-X*, *NEXT* and/or *XEUS*.

5. Conclusion

Using *Chandra* ACIS-I, we have carried out a deep X-ray observation (0.5 – 10 keV) on a typical Galactic region at $(l, b) \approx (28.°5, 0.°0)$ within $\sim$250 arcmin^2, followed by a NIR identification observation with NTT/SOFI at ESO. Main results are summarized below:

1. We have detected 274 new X-ray sources (4 σ confidence) down to $\sim 3 \times 10^{-15}$ erg s^{-1} cm^{-2} in 2 – 10 keV or $\sim 2 \times 10^{-16}$ erg s^{-1} cm^{-2} in 0.5 – 2 keV. Only 26 sources are detected both in the soft and hard bands. In the SOFI field, 83 % of the soft sources are identified in NIR, while only 22 % of the hard sources have NIR conterparts. Most of the soft X-ray sources are considered to be X-ray active stars, while a significant part of the unidentified hard X-ray sources are extragalactic.

2. Only $\sim$ 10 % of the detected X-ray fluxes in the *Chandra* field is accounted for by the sum of point source fluxes. Hence, we conclude Galactic ridge X-ray emission is truly diffuse emission.

3. Soft X-ray sources exhibit thin thermal spectra, characteristics of active stars. Difference between the soft X-ray sources with and without NIR counterparts is only due for a small part to the source distance. It results to a large extent from differences in their intrinsic NIR luminosities. Small number of the hard X-ray sources with NIR counterpart is considered to be Galactic cataclysmic variables, and exhibits a narrow iron emission line at 6.67 keV expected from hot equilibrium plasma.

4. Removing contamination of point X-ray sources, we have precisely measured the Galactic ridge diffuse X-ray emission. The observed diffuse flux is 2.4×10^{-7} ergs cm^{-2} s^{-1} str^{-1} (0.7 – 10 keV). The energy spectrum can be modeled with a two temperature non-equilibrium ionization model, such that the soft and hard component have different plasma parameters and different amounts of interstellar absorption.

5. We have measured the diffuse iron emission line energy as $6.52 \pm^{0.08}_{0.14}$ keV (90 % error). This is significantly lower than what is expected from thermally equilibrium plasma (6.67 keV). This shift of the iron line energy may be explained either by non-equilibrium ionization of the plasma, or hybrid of the 6.4 keV fluorescent line and the 6.67 keV line from equilibrium plasma.

REFERENCES

Bamba, A., Ueno, M., Koyama, K. , & Yamauchi, S. 2001, PASJ, 63, L21

Bélanger, G. et al. 2004, ApJ, 601, L163

Bertin, E. & Arnouts, S. 1996, A&AS, 117, 393

Cox, A. N. 1999, "Allen's Astrophysical Quanties", fourth edition, Springer

Cutri, R. et al. 2005, in preparation

Dame, T. M., Hartmann, D. & Thaddeus, P. 2001, ApJ, 547, 792

Dickey, J. M. & Lockman, F. J. 1990, ARAA, 28, 215

Dogiel, V.A., Inoue, H., Masai, K., Schönfelder, V. & Strong, A. W. 2002, ApJ, 581, 1061

Downes, R., Webbink, R., Shara, M., Ritter, H., Kolb, U., Duerbeck, H. 2001, PASP, 113, 764

Ebisawa, K., Maeda, K., Kaneda, H. & Yamauchi, S. 2001, Science, 293, 1633

Ebisawa, K., Yamauchi, S., Bamba, A., Ueno, M. & Senda, A. 2003, Astron. Nachr. 324, 52

Ezuka, H. & Ishida, M. 1999, ApJS, 120, 277

Forman, W., Jones, C., Cominsky, L., Julien, P., Murray, S., Peters, G., Tananbaum, H. & Giacconi, R. 1978, ApJS, 38 357

Gehrels, N. & Tueller, J. 1993, ApJ, 407, 597

Giacconi, R. et al. 2001, ApJ, 551, 624

Hands, A. D. P., Warwick, R. S., Watson, M. G. & Helfand, D. J. 2004, MNRAS, 351, 31

Harjunpaeae, P. & Mattila, K. 1996, A&A, 305, 920

Hertz, P. & Grindlay, J. E. 1984, ApJ, 278, 137

Hoard, D. W., Wachter, S. Clark, L. L. & Bowers, T. P. 2002, ApJ, 565,511

Kaneda, H., Makishima, K., Yamauchi, S., Koyama, K., Matsuzaki, K. & Yamasaki, N. Y. 1997, ApJ, 491, 638

Koyama, K., Makishima, K., Tanaka, Y. , & Tsunemi, H. 1986, PASJ, 38, 121

Masai, K. 1984, Ap&SS, 98, 367

Masai, K., Dogiel, V.A., Inoue, H., Schönfelder, V. & Strong, A. W. 2002, ApJ, 581, 1071

Minter, A.H., Lockman, F. J., Langston, G. I. & Lockman, J. A. 2001, ApJ, 555, 868

Motch, C., Belloni, T., Buckley, D. et al. 1991, A&A, 246, L24

Mukai, K. & Shiokawa, K. 1993, ApJ, 418, 863

Muno, M. P. et al. 2003, ApJ, 589, 225

Muno, M. P. et al. 2004, ApJ, 613, 326

Murakami, H., Koyama, K. , & Maeda, Y. 2001, ApJ, 558, 687

Popov, S. B., Colpi, M. Prokhorov, M. E., Treves, A. & Turolla, R. 2000, ApJ, 544, L53

Predehl, P. & Schmitt, J. 1995, A&A, 293, 889

Sakano, M., Koyama, K., Murakami, H., Maeda, Y. & Yamauchi, S. 2002, ApJS, 138, 19

Skibo, J. G. et al. 1997, ApJ, 483, L95

Strong, A. W., Bouchet, L., Diehl, R., Mandrou, P., Schönfelder, V. & Teegarden, B. J. 2003, A&A, 411, L447

Sugizaki, M., Mitsuda, K., Kaneda, H., Matsuzaki, K., Yamauchi, S. & Koyama, K. 2001, ApJS, 134, 77

Tanaka, Y., Inoue, H. & Holt, S. S. 1994, PASJ, 46, L37

Tanaka, Y., Miyaji, T. & Hasinger G. 1999, Astron. Nachr., 320, 181

Tanaka, Y. 2002, A&A, 382, 1052

Tanaka, Y., Koyama, K., Maeda, Y. & Sonobe, T. 2000, PASJ, 52, L25

Tanuma, S., Yokoyama, T., Kudoh, T., Matsumoto, R., Shibata, K. & Makishima, K. 1999, PASJ, 51, 161

Tarenghi, M. & Wilson, R. N.; 1989, SPIE, 1114, 302

Ueda, Y. et al. 1999, ApJ, 518, 656

Ueno, M., Bamba, A., Koyama, K. & Ebisawa, K. 2003, ApJ, 588, 338

Valinia, A. & Marshall, F. E. 1998, ApJ, 505, 134

Valinia, A., Kinzer, R. L. & Marshall, F. E. 2000a, ApJ, 534, 277

Valinia, A. et al. 2000b, ApJ, 543, 733

Vuong, M. H., Montmerle, T., Grosso, N., Feigelson, E. D., Verstraete, L. & Ozawa, H. 2003, A&A, 408, 581

Watson, M. G. 1999, in "Annapolis Workshop on Magnetic Cataclysmic Variables", ASP conference series, vol. 157, p. 291

Warwick, R. S., Turner, M. J. L., Watson, M. G. & Willingale, R. 1985, Nature, 317, 218

Weisskopf, M. C., Brinkman, B., Canizares, C., Garmire, G., Murray, S. & Van Speybroeck, L. P. 2002, PASP, 114, 1

Worrall, D. M., Marshall, F. E., Boldt, E. A. & Swank, J. H. 1982, ApJ, 255, 111

Yamasaki, N. et al. 1997, ApJ, 481, 821

Yamauchi, S. & Koyama, K. 1993, ApJ, 404, 620

Yamauchi, S., Kaneda, H. Koyama, K., Makishima, K., Matsuzaki, K., Sonobe, T. Tanaka, Y. & Yamasaki, N. 1996, PASJ, 48, L15

Yamauchi, S. et al. 2002, in the Proceedings of the IAU 8th Asian-Pacific Regional Meeting, Volume II, Edited by S. Ikeuchi, J. Hearnshaw, & T. Hanawa, the Astronomical Society of Japan, p.81
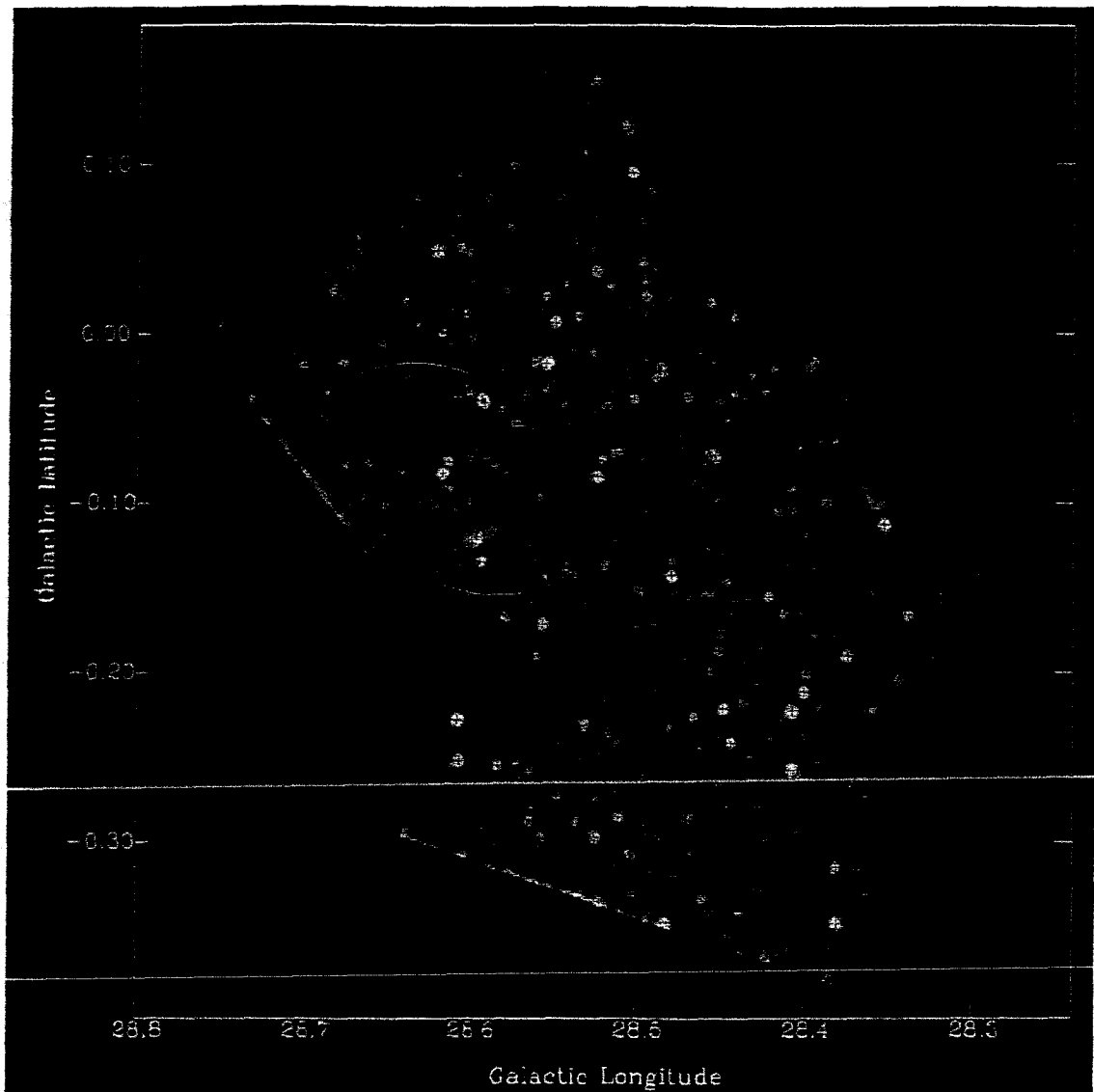
Fig. 1.— Superposed image of the two *Chandra* observations with exposure and vignetting correction (in Galactic coordinates). The upper and lower *Chandra* pointings were made in AO1 and AO2, respectively (each 100 ksec). This is a true-color *Chandra* image where soft X-rays in 0.5 – 2 keV are represented in red, medium X-rays in 2 – 4 keV in green, and hard X-rays in 4 – 8 keV in blue. The image is adaptively smoothed so that both the point sources and the diffuse emission are clearly visible. The 274 detected point sources (Table 1) are marked with crosses. The region including the supernova remnant AX J 1843.8–0352/G28.6–0.1 (Bamba et al. 2001; Ueno et al. 2003) is shown with a yellow ellipse, within which the thermal blob structure CXOU J184357-035441 (Ueno et al. 2003) is marked with a red arrow. Note that the supernova remnant AX J 1843.8–0352/G28.6–0.1, which exhibits non-thermal energy spectrum (Bamba et al. 2001; Ueno et al. 2003), is more prominent in hard X-rays ("bluish" in this representation) than in soft X-rays.
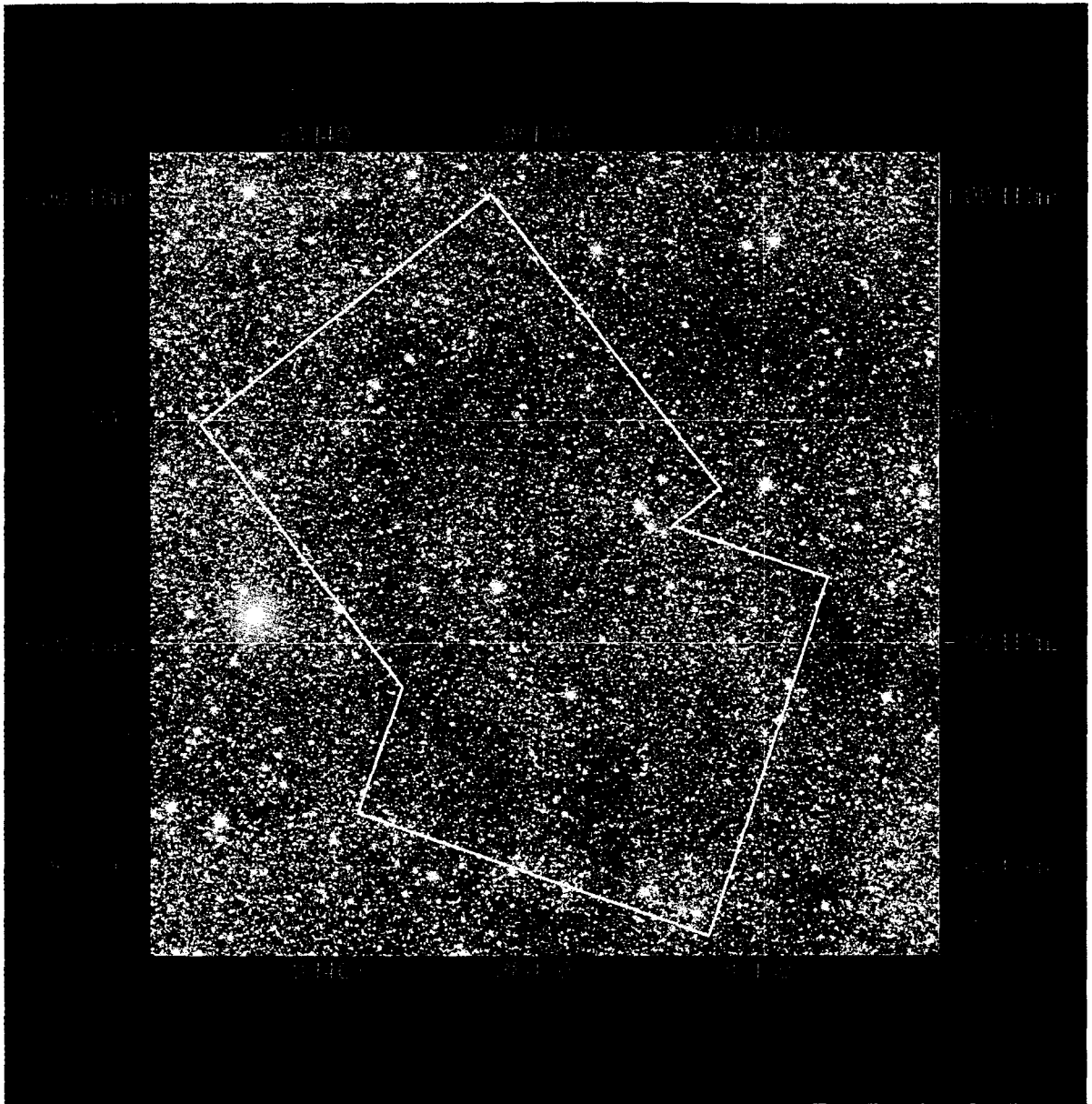
Fig. 2.— 2MASS true color image of the region including our *Chandra* field (in Galactic coordinates). The *Chandra* field of view is drawn, and the *Chandra* sources are marked in red, green or blue, for soft, medium and hard sources, respectively. For the definition of the source spectral hardness, see Section 3.2.
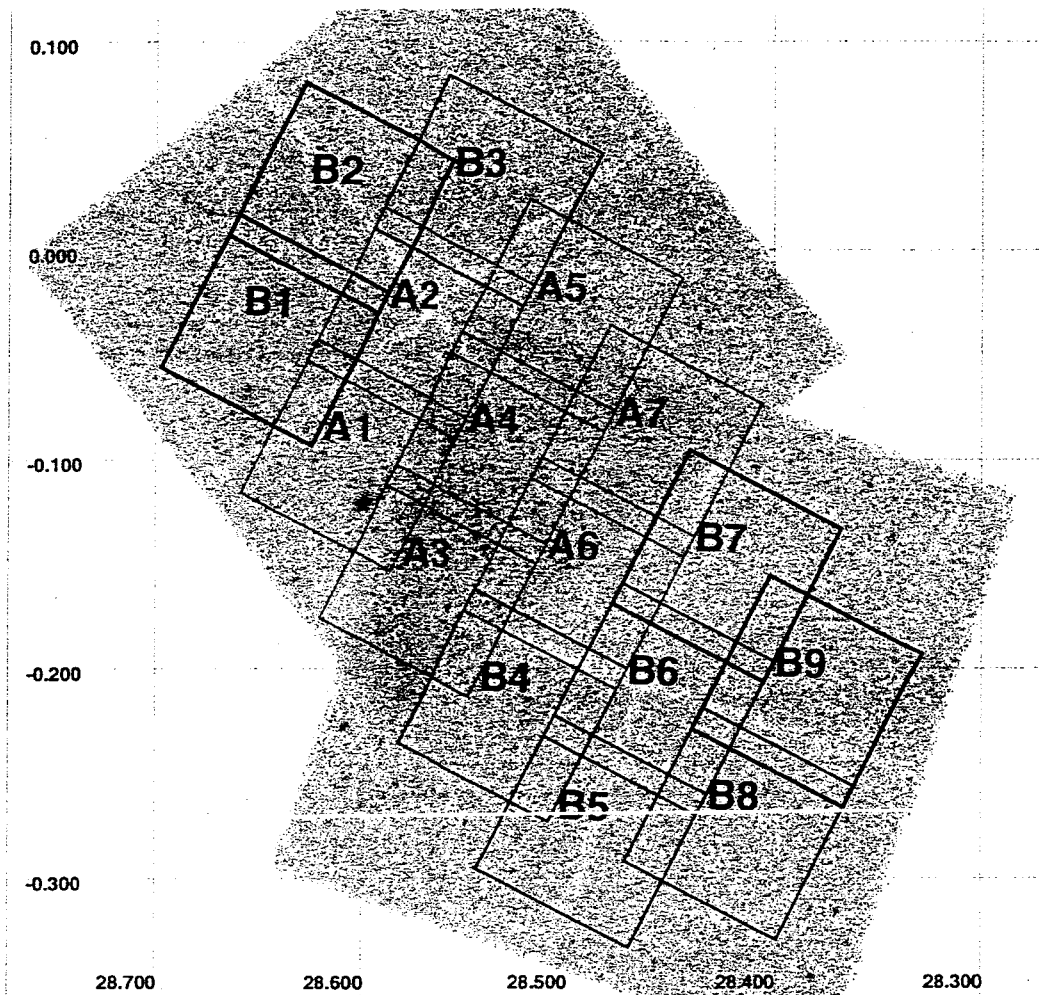
Fig. 3.— SOFI pointing positions on the *Chandra* image (without exposure correction) in Galactic coordinates. Without exposure correction, the AO1 and AO2 overlapping fields and CCD gaps are noticeable (compare with Fig. 1).
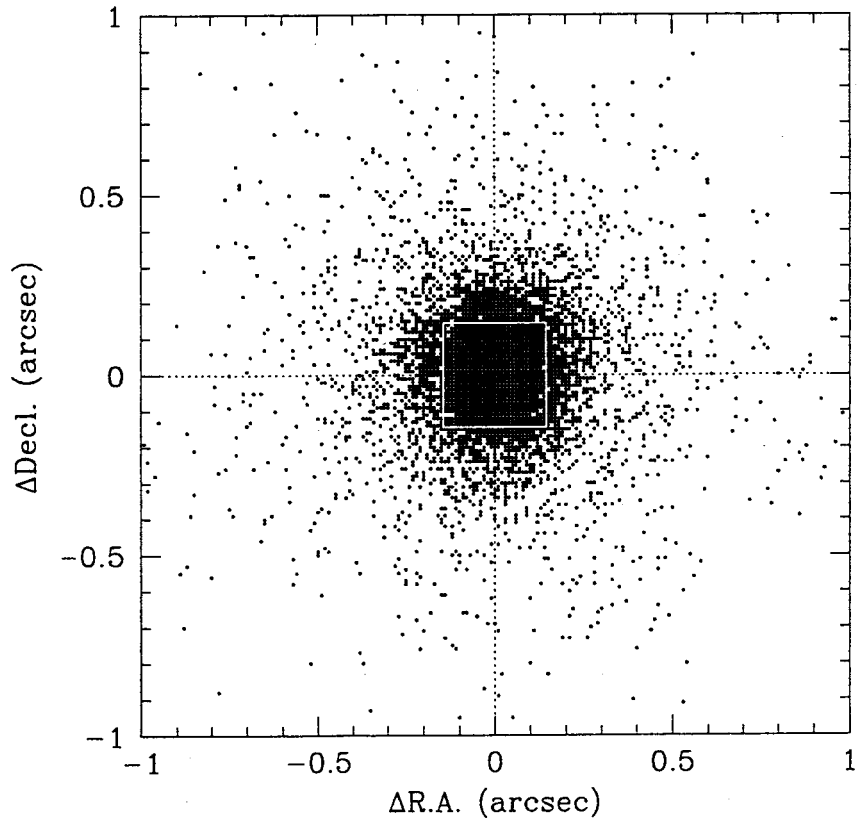
Fig. 4.— For all the 2MASS sources in the SOFI field of view, relative position of the nearest SOFI source (after astrometric correction) is plotted. The central square indicates the SOFI pixel size (0."2884 × 0."2884). Standard deviation of the positional shift between 2MASS and SOFI is 0."2 in R.A. and Decl.
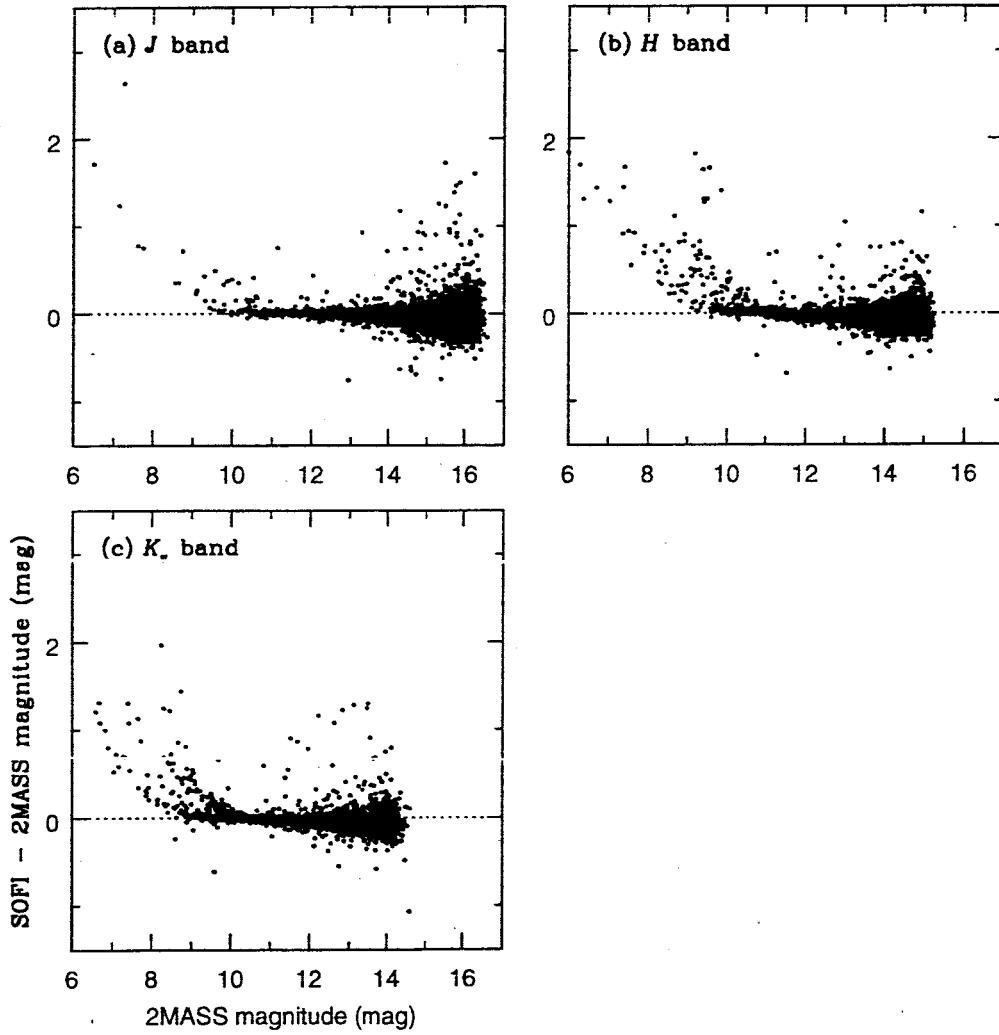
Fig. 5.— Correlation of the J, H and K_S magnitudes of the sources detected by both 2MASS and SOFI. Difference of the magnitudes is plotted as a function of the 2MASS magnitudes.
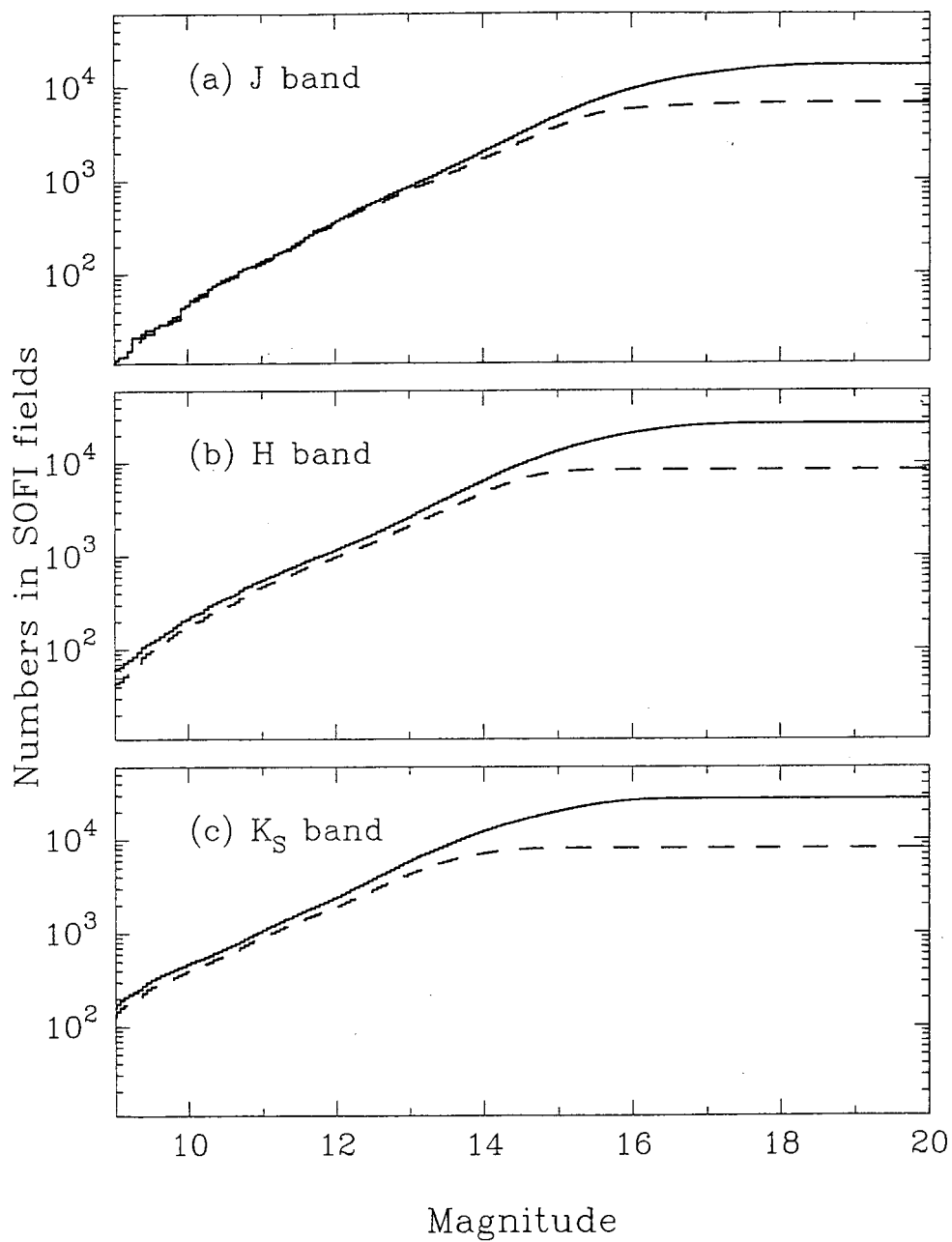
Fig. 6.— Cumulative histograms of the number of SOFI sources (*solid line*) detected in J, H and K_S bands, as a function of the SOFI magnitudes. Number of 2MASS sources in the SOFI fields are also shown with dashed line. Sources detected in two or three bands are counted in each detected band.
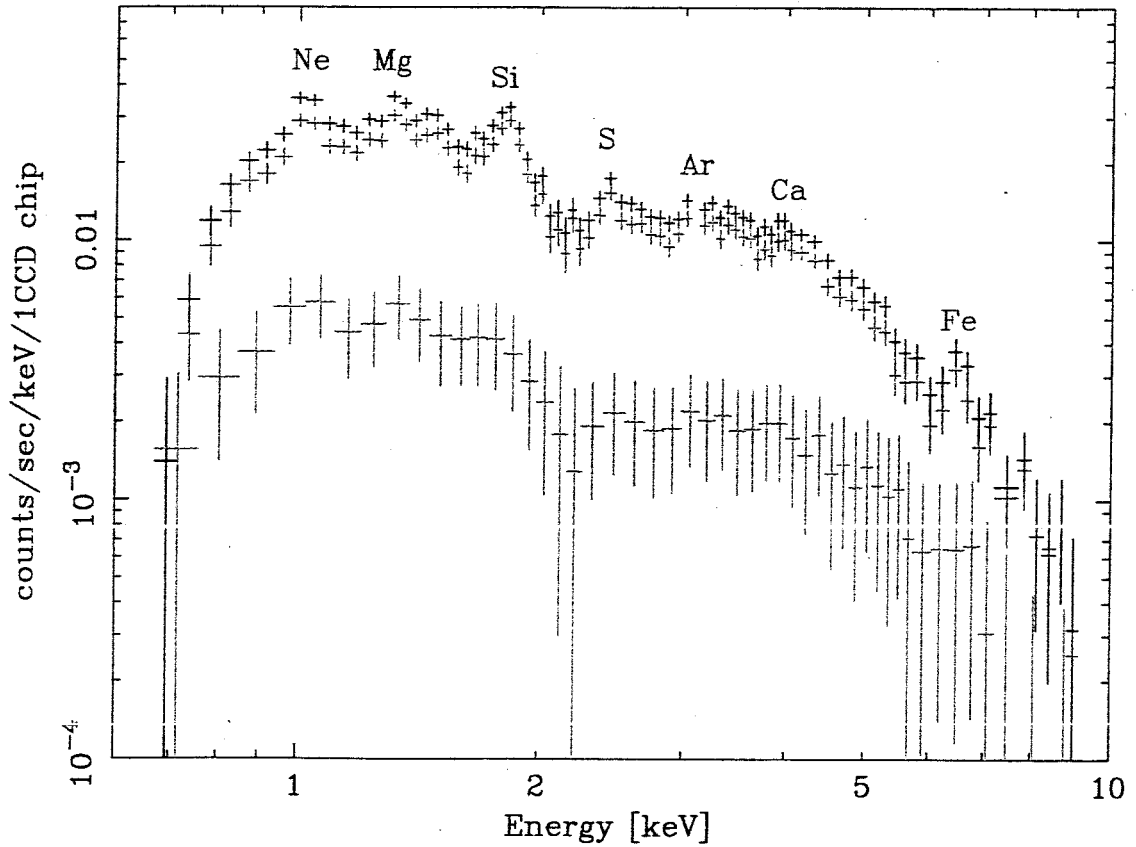
Fig. 7.— Energy spectra of the total X-rays in the field of view (black; the AX J 1843.8–0352/G28.6–0.1 region in Fig. 1 is excluded), of the sum of all the point sources (green), and of their difference, namely, the Galactic diffuse emission (red). It is found that ∼ 90 % of the X-ray emission is from the diffuse emission, with which emission lines from highly ionized heavy elements are associated (prominent emission lines are annotated with element names). The ordinate is normalized with the average counting rate per CCD chip.
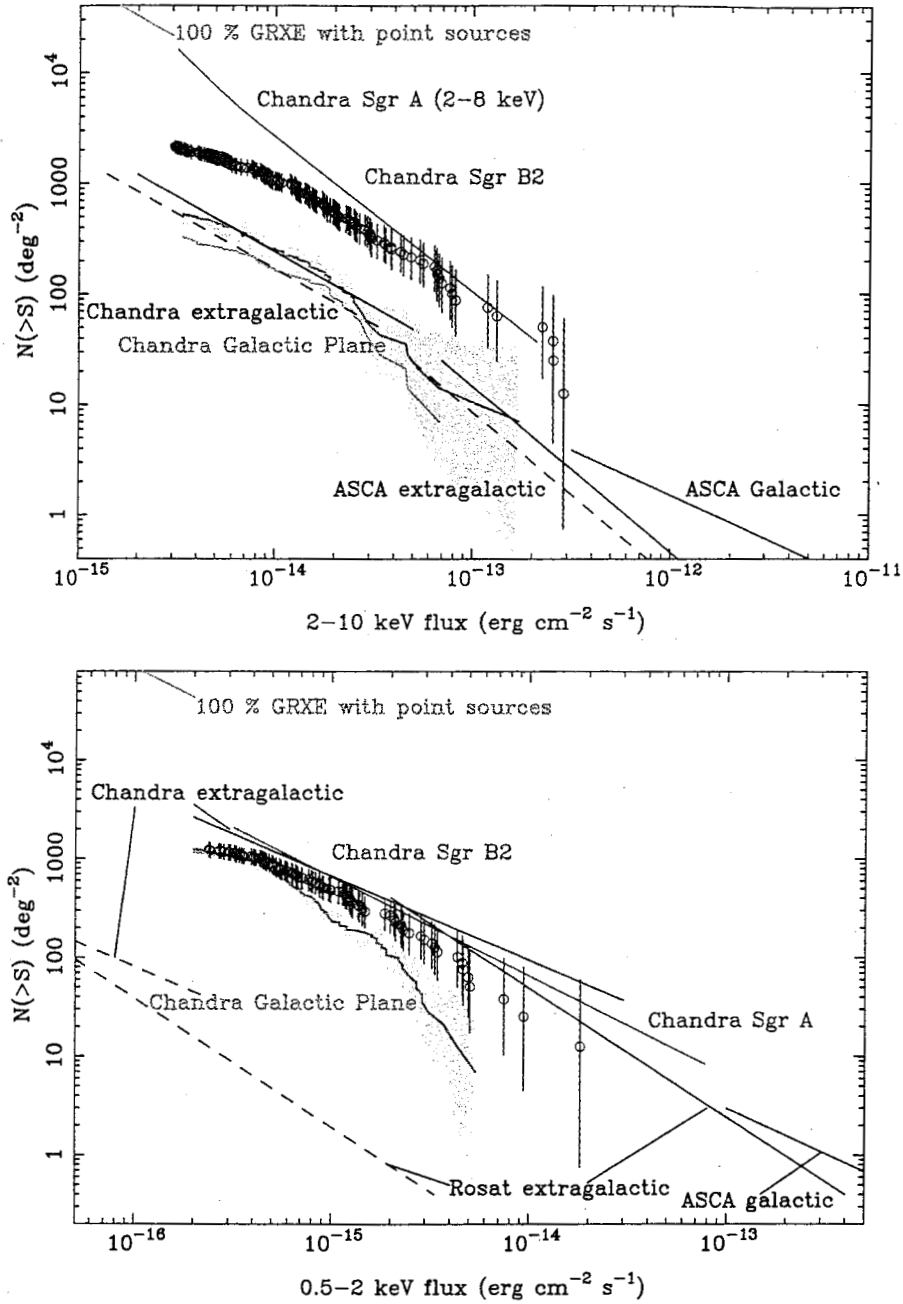
Fig. 8.— The $\log N - \log S$ curves of the point sources detected in our *Chandra* Galactic plane field in 2 – 10 keV (top) and 0.5 – 2 keV (bottom). They are indicated in red lines, and the 90 % error regions are shown in yellow. Also the $\log N - \log S$ curves of only the sources having the near infrared counterparts are shown in cyan (in the soft band, it is almost completely overlapped with red-line, and barely seen only at the lowest flux). In addition, number of the hypothetical point sources whose sum would account for the 100 % of the Galactic ridge X-ray emission at a given point source flux is indicated (in green) below our detection limits. Together, other $\log N - \log S$ relations are shown for the bright *ASCA* Galactic sources (Sugizaki et al. 2001), *Chandra* Galactic center Sgr B2 and Sgr A (Muno et al. 2003), and extragalactic point sources detected with *ASCA* (Ueda et al. 1999), *ROSAT* and *Chandra* (Giacconi et al. 2001). For the extragalactic sources, both the original $\log N - \log S$ curves at high Galactic latitudes (black solid lines) and the ones expected
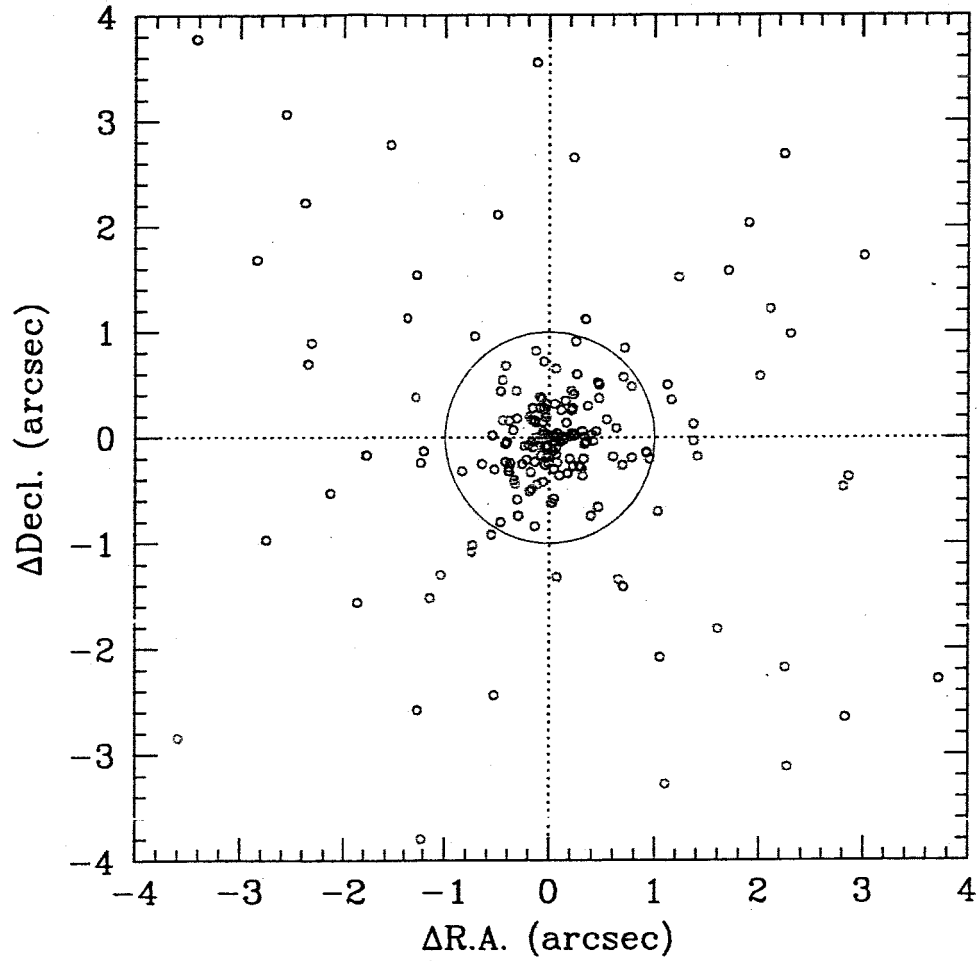
Fig. 9.— For all the *Chandra* sources detected in the fields covered by SOFI, positional offsets of the nearest SOFI sources are plotted. Red, green and blue are soft, medium and hard X-ray sources, respectively. We consider sources within 1″ (central circle) as the counterparts. It is obvious that soft X-ray sources are more likely to have NIR counterparts than harder X-ray sources (see also Table 3).
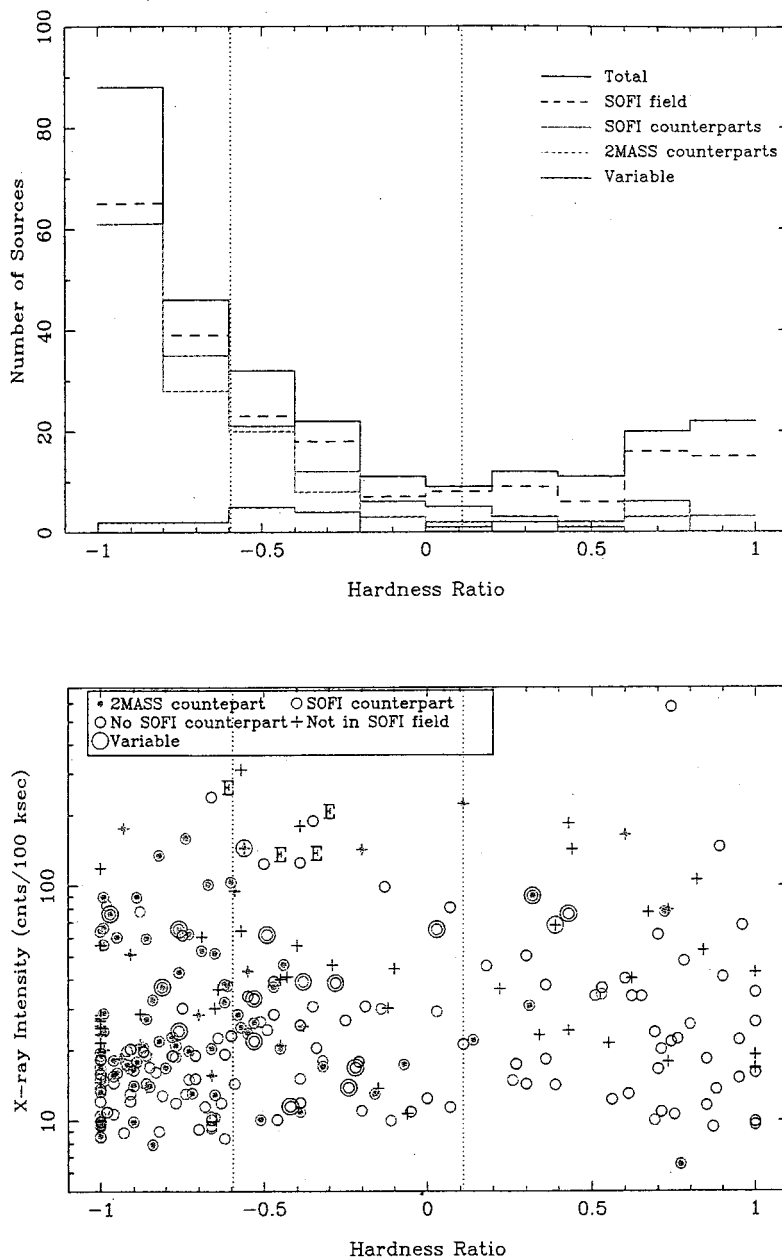
Fig. 10.— Histogram of the number of sources as a function of the spectral hardness ratio (HR) (top) and HR vs. the count rate (bottom). In the top panel, the dashed line indicates the number of sources within the SOFI fields (Fig. 3), and the red line shows the sources having the SOFI near-infrared counterpart. The green line indicates the number of sources having 2MASS counterpart, and the blue line indicates the number of variable sources (Section 3.5.3). In the bottom panel, the sources outside of the SOFI field are shown with crosses, and those inside are with circles: black circles indicate the sources without SOFI counterparts, while red circles are those having the SOFI counterparts. In addition, sources having the 2MASS counterparts are marked with green dots, and variable sources are marked with blue circle. The vertical dotted lines in both figures indicate the boundaries we defined between the soft and medium sources ($HR = -0.595$), and the medium and hard sources ($HR = 0.11$). Source marked with "E" (Sources 208, 210, 213 and 126) in the bottom panel are parts of the extended feature CXOU J184357-035441 (Section 2.2; Ueno et al. 2003)
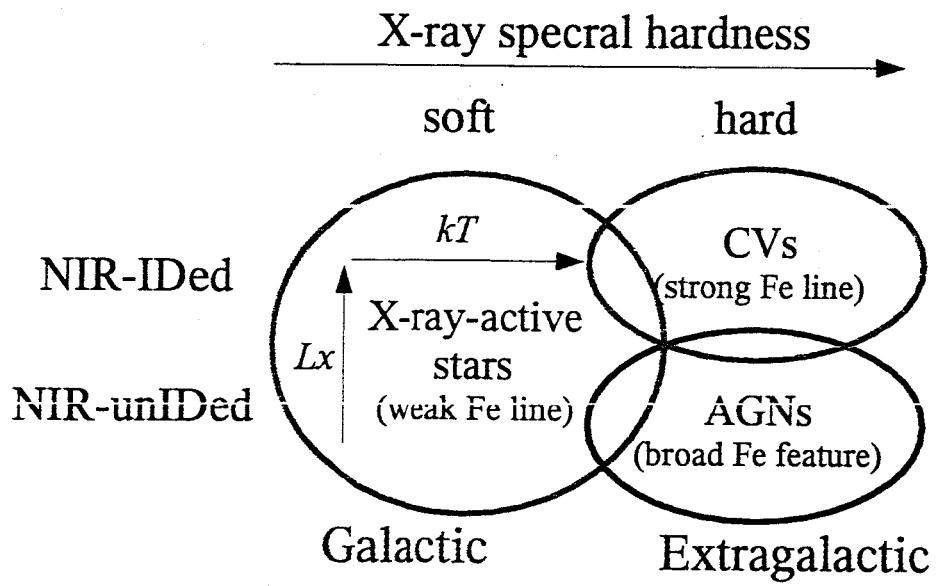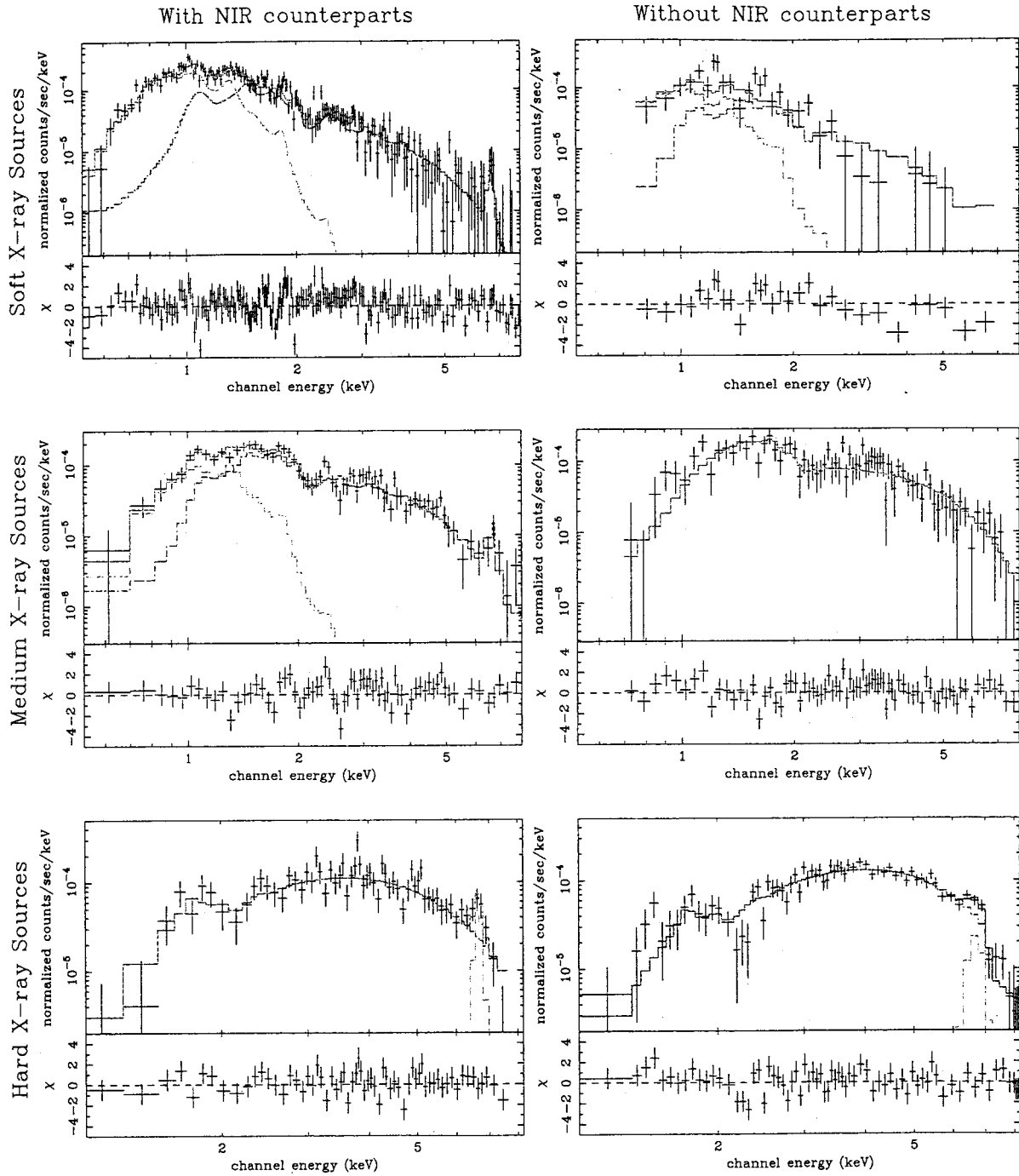
Fig. 12.— Composite energy spectra and model fitting of the point sources grouped by the X-ray spectral hardness and absence or presence of the NIR counterpart. Those having the NIR counterpart are in the left-hand side, and those without the NIR counterpart are in the right-hand side. The top two panels are the soft source spectra, the middle ones are the medium, and the bottom ones the hard. See the text (section 3.5.2) for the fitting models.
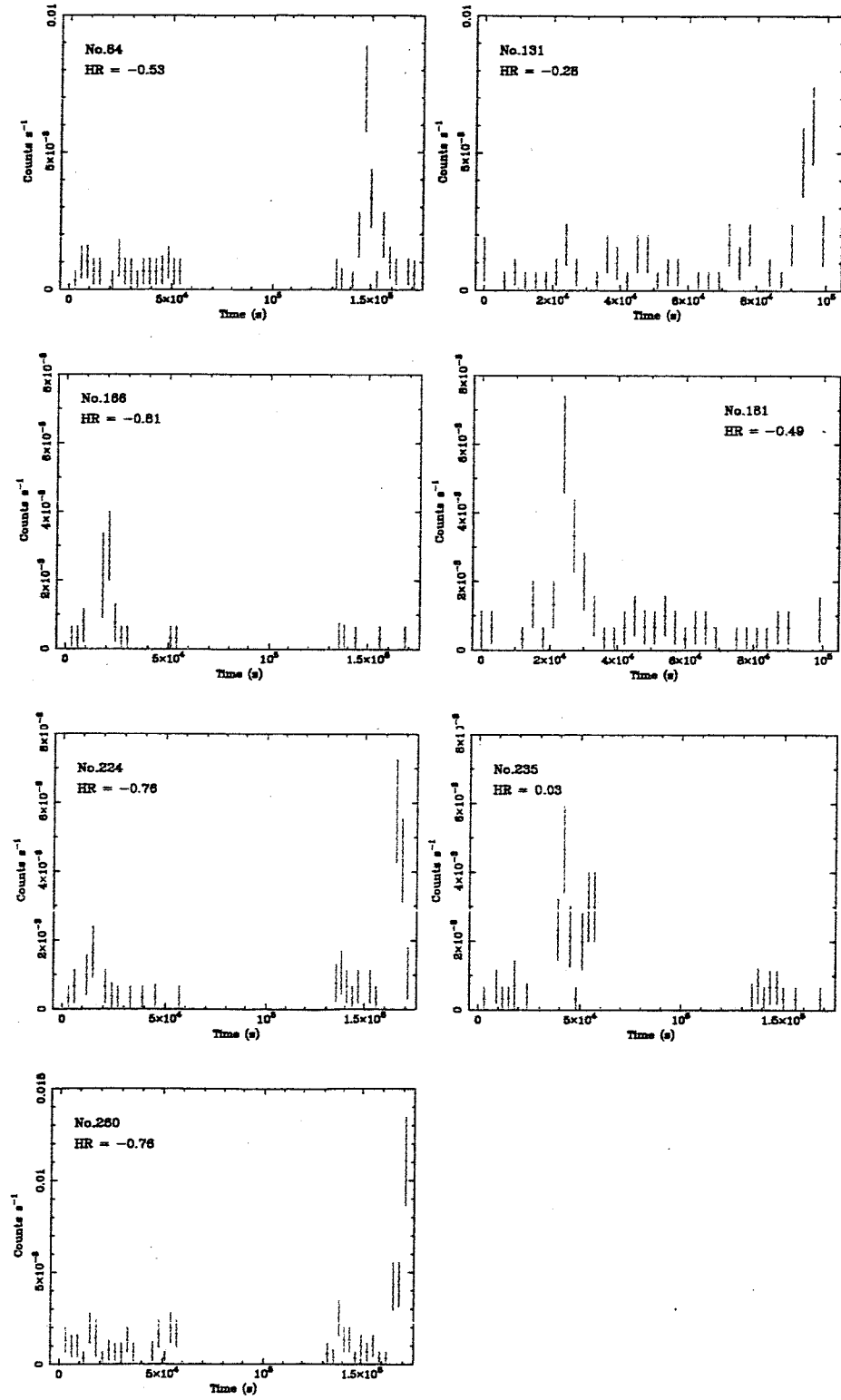
Fig. 13.— Light curves of the seven variable sources exhibiting flare-like phenomena.

Chandra GRXE iron line
Single line model
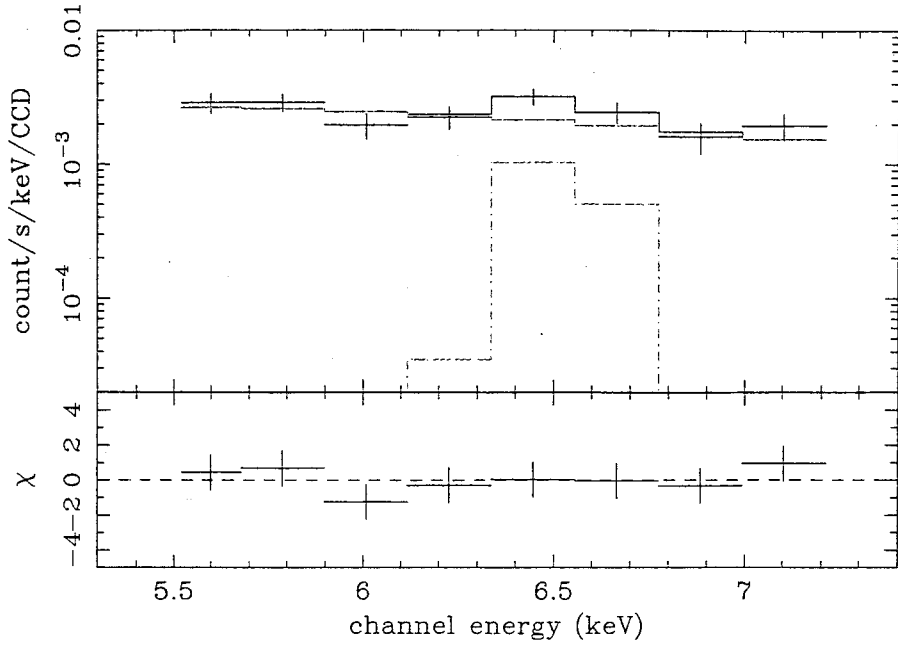
Chandra GRXE iron line
Three line model
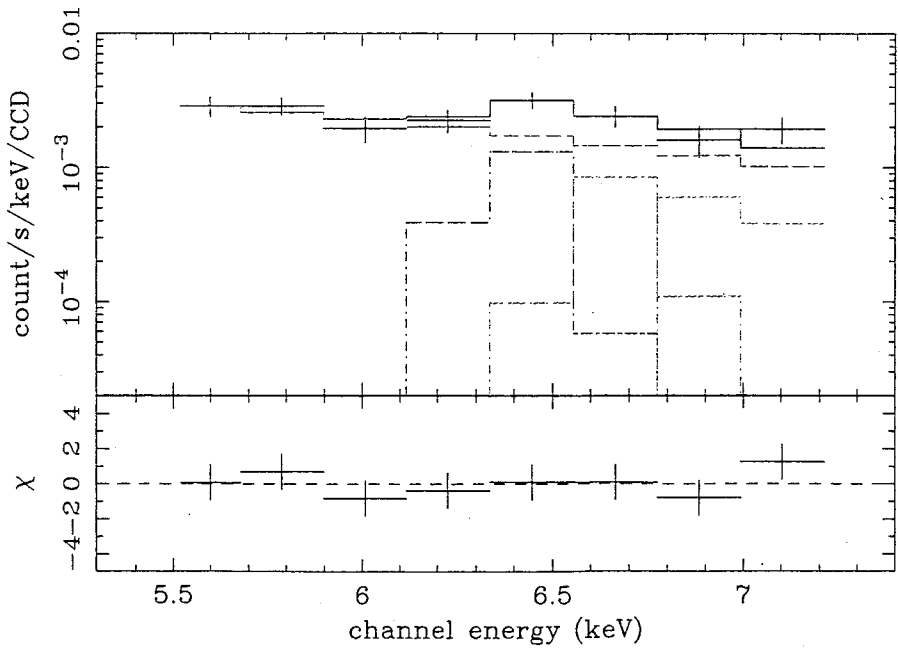
Fig. 14.— The iron line from the Galactic Ridge diffuse X-ray Emission fitted with a single line (top) or three lines (bottom; differentiated with different colors). Both models fit the observed spectrum equally well.

Chandra GRXE low energy lines
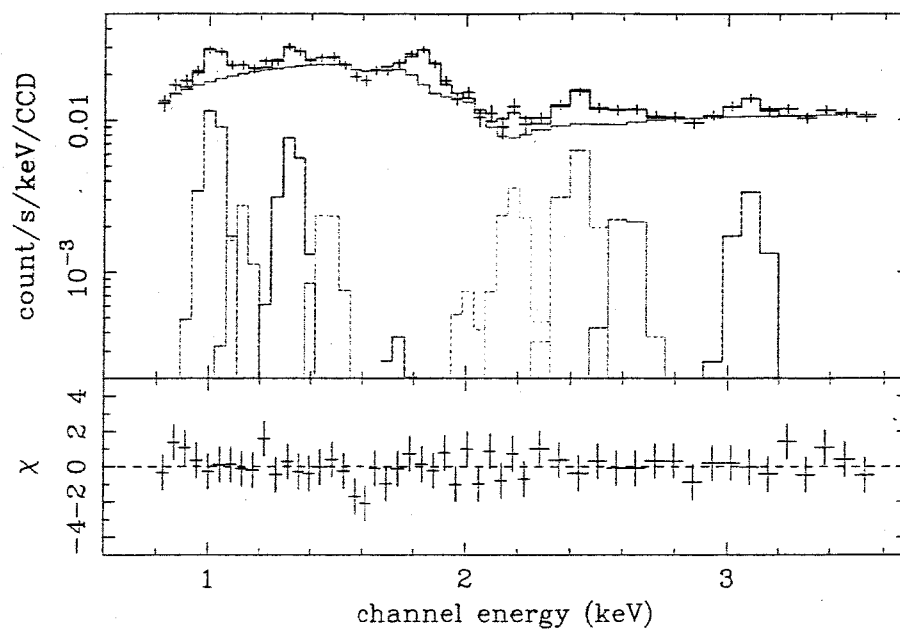
Fig. 15.— Emission lines from the Galactic Ridge diffuse X-ray Emission in the soft energy band. Eleven gaussians (differentiated with different colors) are put with a power-law continuum.

Chandra Galactic Diffuse Two NEI model fit
Fixed abundances
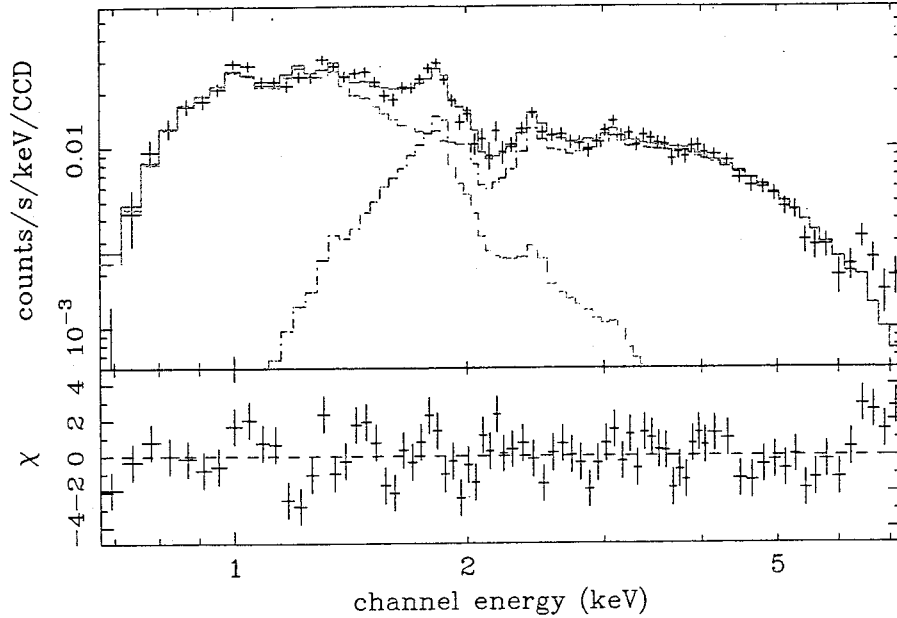
Chandra Galactic Diffuse Two NEI model fit
Variable abundances
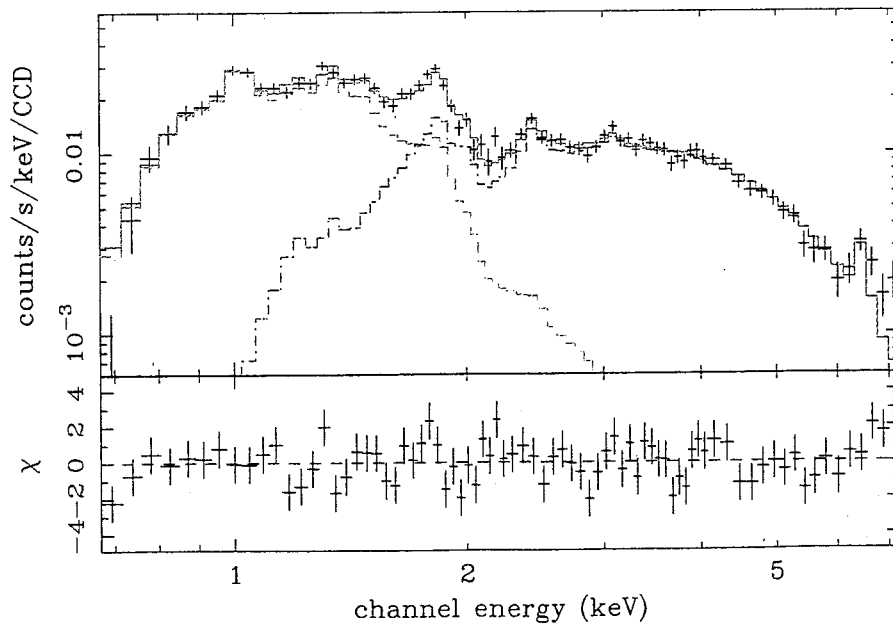
Fig. 16.— Spectral fitting of the Galactic diffuse emission with a two component NEI model (Masai 1984) with fixed abundances for each component (top) or variable abundances (bottom). Note that the iron line ($\sim$ 6.7 keV) and neon line ($\sim$ 1.0 keV) features are fitted in the bottom figure, but not in the top.

GRXE model (with and without absorption)
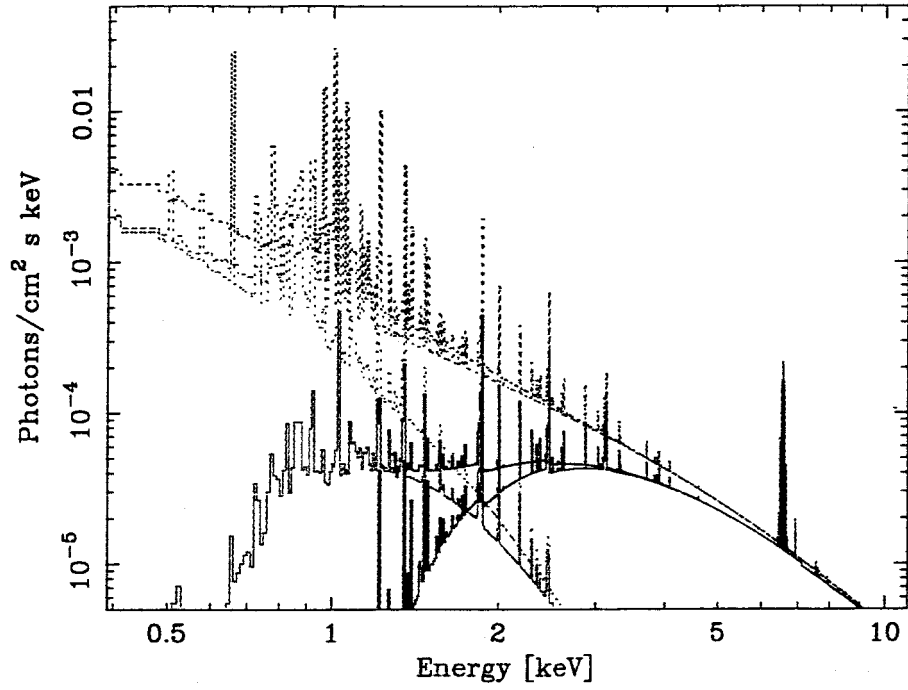
Fig. 17.— Best fit spectral model used in Fig. 16 including interstellar absorption (solid lines) and removing the absorption (dotted lines). Hard component is drawn in blue, soft component is in red, and total is in black.
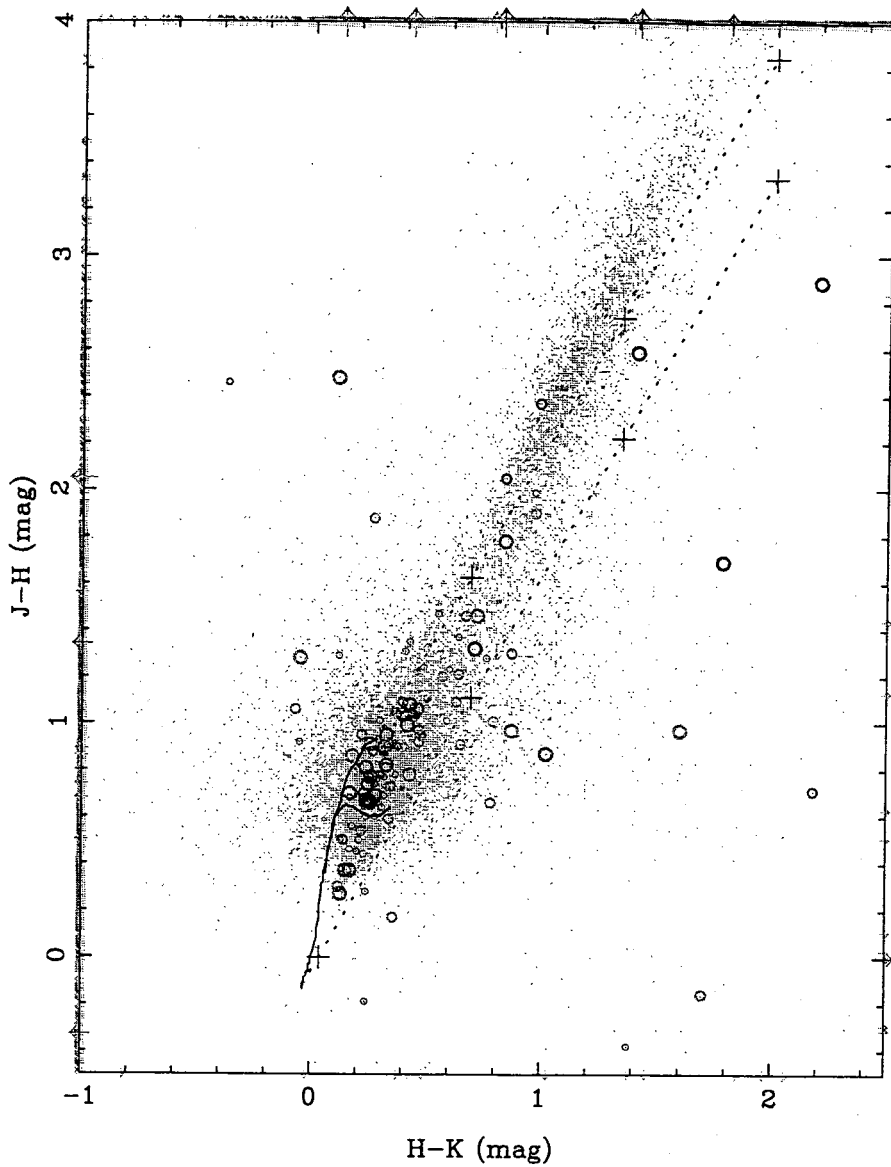
Fig. 18.— NIR color-color diagram of all the SOFI sources (gray) and the *Chandra* sources with NIR counterparts (red, green and blue circles for soft, medium and hard sources, respectively). The symbol size for *Chandra* sources is approximately proportional to the X-ray counting rates. Solid curves indicate the loci for dwarfs (main sequence stars) and giants, and dotted lines show the reddening (towards upper-right), such that distance between the crosses correspond to $A_V = 10$ mag (data taken from Cox 1999). Sources detected only in two bands are marked at the border of the graph. Note that there are significant number of sources which cannot be plotted in this diagram because they are detected only in one band.
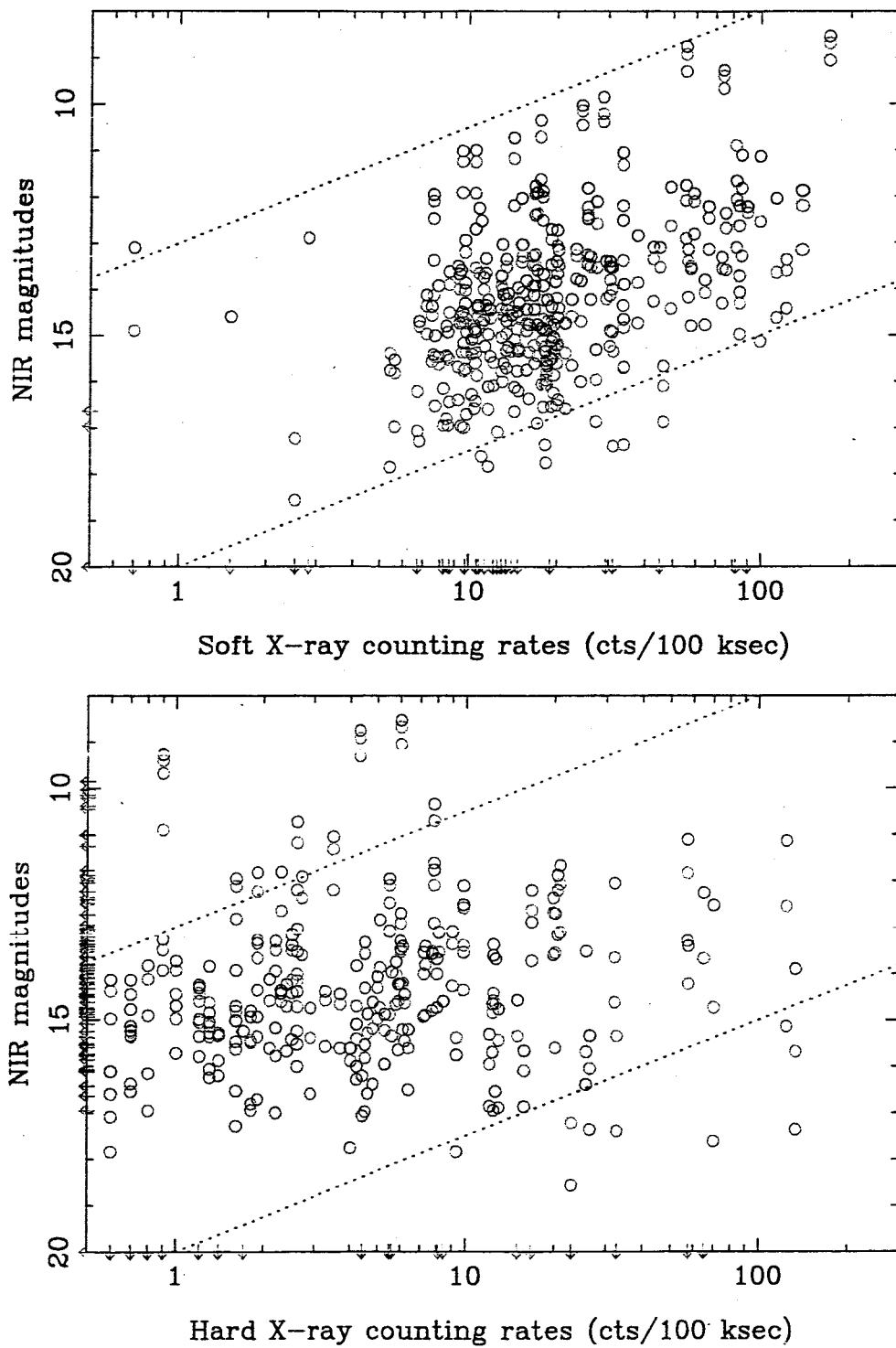
Fig. 19.— Correlation between the X-ray counting rates (top = 0.5 – 2 keV band, bottom= 2 – 10 keV band) and the NIR magnitudes (red=J, green =H and blue = K_S). The black dotted lines indicate the slopes for the sources with the constant luminosities at different distances.
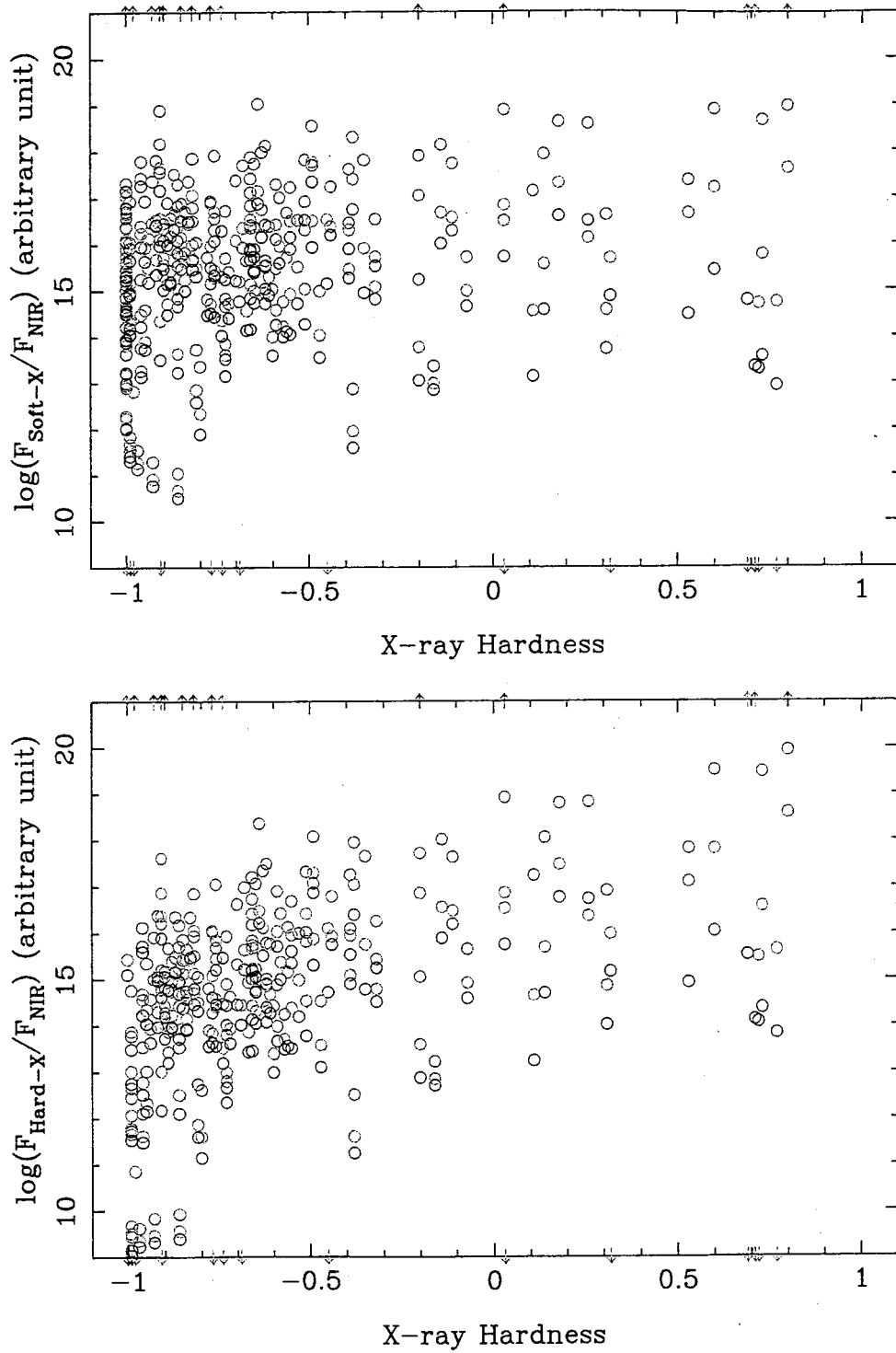
Fig. 20.— X-ray spectral hardness versus the X-ray and NIR flux ratio. Top panel gives the soft X-ray flux over NIR flux ratio, and the bottom is for the hard X-ray flux. Red, green and blue colors indicate J, H and K_S band fluxes, respectively.

Table 1. Detected Source List

ID[a]	AO	R.A. (hh:mm:ss.ss) (J2000)	Dec. (d:mm:ss.s) (J2000)	Error (arcsec)	Significance (σ) Total/Soft/Hard	Normalized counts (cnts/100ks) Total/Soft/Hard	Hardness (H–S)/(H+S)	Flux (ergs s^{-1} cm^{-2}) 0.5–2keV/2–10keV	ID[b]	NIR counterpart separation (arcsec)	J[c] (mag)	H[c] (mag)	K_S[c] (mag)
1	2	18:42:51.77	−3 51 11.2	0.86	5.5/5.1/0.0	27.3/27.1/0.0	−1.00 ± 0.09	4.0E-16/1.6E-16	OoF	...	...	...	...
2[T]	2	18:42:53.53	−3 49 19.6	0.93	0.9/3.0/6.5	67.7/21.3/48.8	0.39 ± 0.12	3.5E-16/1.0E-14	OoF	...	...	...	...
3[T]	2	18:42:58.30	−3 53 28.1	0.49	11.3/0.0/11.4	79.2/11.0/70.0	0.73 ± 0.08	4.2E-17/3.1E-14	J18426832-0353371	1.00	17.62	14.73	12.53
4[T]	2	18:43:00.41	−3 53 48.9	0.36	19.0/18.5/6.0	144.7/112.9/32.1	−0.50 ± 0.07	2.5E-15/1.0E-14	J18430043-0353486	0.36	14.62	13.65	12.05
5	2	18:43:01.50	−3 50 47.3	0.69	5.0/0.0/5.1	17.8/2.5/15.8	0.73 ± 0.20	8.8E-18/6.4E-15	OoF	...	...	...	...
6	2	18:43:01.83	−3 54 42.4	0.48	7.4/0.7/2.0	45.9/29.8/16.3	−0.29 ± 0.15	9.5E-16/3.9E-15	OoF	...	...	...	...
7	2	18:43:06.14	−3 54 54.8	0.43	4.1/4.6/0.0	20.9/15.2/5.8	−0.45 ± 0.21	4.3E-16/1.8E-15	OoF	...	...	...	...
8	2	18:43:06.88	−3 55 37.0	0.35	8.1/8.0/4.0	30.1/17.0/13.2	−0.12 ± 0.19	2.1E-16/0.2E-15	OoF	...	...	...	...
9	2	18:43:07.25	−3 49 55.2	0.55	5.2/8.2/0.0	28.2/28.1/0.0	−1.00 ± 0.08	8.3E-16/3.4E-16	OoF	...	...	...	...
10	2	18:43:07.27	−3 48 58.4	0.75	4.1/0.0/4.0	16.8/0.0/17.2	1.00 ± 0.13	1.1E-17/8.0E-15	No	...	...	...	...
11	2	18:43:07.98	−3 53 17.1	0.40	8.1/7.2/0.0	30.6/18.3/12.4	−0.19 ± 0.19	2.3E-16/6.8E-15	OoF	...	...	...	...
12	2	18:43:08.73	−3 50 01.8	0.53	4.6/3.5/2.4	10.7/6.3/5.7	−0.06 ± 0.32	4.0E-17/1.2E-15	No	...	...	...	...
13	2	18:43:10.86	−3 55 35.5	0.38	4.3/0.3/0.0	20.2/19.3/0.9	−0.91 ± 0.10	5.0E-16/2.0E-16	OoF	...	...	...	...
14	2	18:43:11.41	−3 59 50.1	0.46	8.1/7.6/1.8	39.9/28.9/10.5	−0.45 ± 0.15	7.2E-16/3.0E-16	OoF	...	...	...	...
15	2	18:43:11.81	−3 58 23.7	0.27	7.2/8.8/0.0	26.7/26.7/0.0	−1.00 ± 0.08	7.0E-16/2.8E-16	OoF	...	...	...	...
16	2	18:43:12.15	−3 48 10.2	0.72	3.6/6.0/0.0	21.1/19.7/1.3	−0.88 ± 0.15	7.2E-16/2.9E-16	J18431219-0348167	0.93	15.28	14.62	13.84
17	2	18:43:12.42	−3 57 36.8	0.49	4.3/4.0/0.0	15.6/13.0/2.6	−0.66 ± 0.22	3.8E-16/1.0E-15	J18431239-0357363	0.61	16.00	14.01	13.04
18	2	18:43:12.87	−3 50 42.0	0.55	4.6/4.9/0.0	14.8/14.8/0.0	−1.00 ± 0.15	4.8E-16/1.9E-16	OoF	...	...	...	...
19	2	18:43:12.92	−3 49 36.8	0.49	5.9/6.8/0.0	25.4/25.3/0.0	−1.00 ± 0.09	7.9E-16/3.2E-16	J18431289-0349389	0.36	13.47	12.93	12.48
20	2	18:43:13.36	−4 02 30.1	0.80	5.2/5.5/0.0	29.5/25.3/4.3	−0.71 ± 0.15	8.2E-16/3.4E-15	OoF	...	...	...	...
21	2	18:43:13.77	−3 57 07.4	0.35	6.4/6.9/0.0	20.1/20.0/0.1	−0.99 ± 0.11	5.9E-16/2.4E-16	J18431378-0357073	0.28	13.66	13.57	12.73
22	2	18:43:14.45	−3 52 11.5	0.32	4.2/4.3/0.0	12.7/12.7/0.0	−1.00 ± 0.17	2.0E-16/1.1E-16	No	...	...	...	...
23	2	18:43:14.97	−3 58 12.8	0.45	4.9/3.8/0.0	16.3/10.5/5.8	−0.29 ± 0.26	4.1E-16/1.7E-15	OoF	...	...	...	...
24	2	18:43:15.29	−3 54 19.5	0.17	9.1/9.7/0.0	24.1/24.2/0.1	−0.99 ± 0.08	6.9E-16/2.8E-16	S687/J18431530-0354190	0.38	10.45	10.15	10.03
25	2	18:43:15.29	−3 56 17.2	0.22	10.6/10.7/0.0	30.1/26.3/3.8	−0.75 ± 0.13	8.6E-16/3.6E-15	No	...	...	...	...
26	2	18:43:15.40	−3 50 49.1	0.34	4.5/5.0/0.0	13.9/12.9/1.0	−0.86 ± 0.15	6.1E-16/2.5E-16	J18431539-0350483	0.74	14.43	13.93	13.72
27	2	18:43:15.54	−3 47 58.5	0.67	4.7/0.0/4.9	21.4/4.7/15.9	0.55 ± 0.21	1.3E-16/4.0E-15	OoF	...	...	...	...
28	2	18:43:15.81	−3 56 40.4	0.42	4.3/0.0/2.9	13.7/8.5/0.3	−0.15 ± 0.28	7.3E-17/2.2E-15	OoF	...	...	...	...
29	2	18:43:17.43	−3 56 00.2	0.22	5.9/3.9/2.8	13.0/7.6/5.5	−0.16 ± 0.30	1.3E-16/3.9E-15	S1031/J18431748-0355697	0.90	12.48	12.10	11.96
30	2	18:43:17.43	−3 57 32.7	0.23	7.0/7.4/0.0	19.8/19.1/0.7	−0.92 ± 0.11	5.5E-16/2.2E-16	S1018	0.13	16.54	15.25	15.13
31	2	18:43:17.47	−3 48 52.6	0.40	5.3/5.9/0.0	18.4/18.4/0.0	−1.00 ± 0.12	4.9E-16/2.0E-16	S1038	0.03	16.06	15.78	15.54
32	2	18:43:17.97	−3 47 14.9	0.82	3.6/4.5/0.0	19.6/19.5/0.0	−1.00 ± 0.12	4.5E-16/1.8E-16	OoF	...	...	...	...
33	2	18:43:18.18	−3 47 32.4	0.89	3.0/4.0/0.0	14.8/14.5/0.0	−1.00 ± 0.18	4.1E-16/1.7E-16	OoF	...	...	...	...
34	2	18:43:18.41	−4 00 54.9	0.77	3.6/4.1/0.0	9.7/9.7/0.0	−1.00 ± 0.23	4.2E-16/1.7E-16	OoF	...	...	...	...
35	2	18:43:18.59	−3 58 52.1	0.35	5.8/6.0/0.0	19.5/19.5/0.0	−1.00 ± 0.11	4.6E-16/1.9E-16	S1360	0.36	15.86	15.08	14.77
36	2	18:43:18.73	−3 54 25.2	0.20	5.1/3.3/0.0	11.0/6.7/4.4	−0.20 ± 0.31	7.3E-17/2.2E-15	S1398	0.22	17.07	16.21	...
37	2	18:43:18.95	−3 53 27.3	0.24	4.4/4.2/0.0	12.8/11.0/1.2	−0.81 ± 0.21	4.3E-16/1.7E-16	S1479	0.74	14.98	14.42	14.24
38	2	18:43:19.01	−3 59 33.4	0.38	8.8/0.0/8.6	33.9/6.4/27.4	0.62 ± 0.14	1.8E-17/1.3E-14	No	...	...	...	...
39	2	18:43:19.22	−3 57 31.9	0.28	4.7/4.8/0.0	13.0/11.3/1.7	−0.74 ± 0.21	3.4E-16/1.4E-15	S1544	0.73	...	...	15.24
40	2	18:43:19.47	−4 01 36.9	0.73	3.3/5.1/0.0	19.1/19.1/0.0	−1.00 ± 0.12	5.5E-16/2.2E-16	OoF	...	...	...	...
41	2	18:43:19.61	−3 55 02.1	0.25	3.8/4.2/0.0	8.9/8.6/0.3	−0.93 ± 0.22	2.3E-16/9.2E-17	S1652	0.81	10.44	15.53	...
42	2	18:43:20.55	−3 48 59.9	0.24	8.1/0.0/8.7	26.3/0.0/26.3	1.00 ± 0.08	2.1E-17/1.5E-14	No	...	...	...	...
43	2	18:43:20.56	−3 49 03.3	0.31	9.1/0.0/10.1	35.2/0.0/35.3	1.00 ± 0.06	2.0E-17/1.5E-14	No	...	...	...	...
44	2	18:43:20.86	−3 52 46.5	0.11	20.6/8.3/14.0	50.2/17.6/32.7	0.30 ± 0.14	3.5E-16/1.1E-14	No	...	...	...	...
45	2	18:43:21.10	−3 52 15.0	0.16	4.7/0.0/4.7	9.4/0.6/8.6	0.87 ± 0.21	4.7E-18/3.4E-15	No	...	...	...	...
46	2	18:43:21.11	−3 54 30.0	0.20	5.0/0.0/4.2	10.0/1.5/8.4	0.09 ± 0.26	6.4E-18/4.6E-15	S2107	0.21	...	...	...
47	2	18:43:21.22	−3 49 31.2	0.37	9.0/11.5/0.0	42.8/37.6/5.1	−0.76 ± 0.10	9.6E-16/4.0E-15	S2159/J18432128-0349314	0.97	14.74	13.87	14.60
48	2	18:43:21.37	−4 01 02.9	0.27	26.1/12.0/22.0	184.7/52.7/131.0	0.43 ± 0.07	1.1E-15/3.4E-14	OoF	...	...	...	...
49	2	18:43:21.62	−3 55 28.0	0.23	4.5/4.8/0.0	9.8/9.7/0.0	−1.00 ± 0.22	5.0E-16/2.0E-16	S2284	0.24	14.03	14.62	12.85

Table 1—Continued

ID[a]	AO	R.A. (hh:mm:ss.ss) (J2000)	Dec. (d:mm:ss.s)	Error (arcsec)	Significance (σ) Total/Soft/Hard	Normalized counts (cnts/100ks) Total/Soft/Hard	Hardness (H-S)/(H+S)	Flux (ergs s⁻¹ cm⁻²) 0.5-2keV/2-10keV	ID[b]	NIR counterpart seperation (arcsec)	J[c] (mag)	H[c] (mag)	K_S[c] (mag)
50	2	18:43:21.76	-4 00 39.6	0.53	4.9/5.7/0.0	18.4/17.9/0.5	-0.94 ±0.12	6.1E-16/2.5E-16	J18432180-0400395	0.73	14.88	14.24	13.93
51	2	18:43:21.81	-3 53 03.3	0.19	8.3/8.0/0.0	18.7/16.5/2.2	-0.77 ±0.17	4.0E-16/1.7E-15	S2354/J18432182-0353031	0.24	13.94	13.49	13.29
52	2	18:43:22.09	-3 54 26.4	0.17	7.4/7.5/0.0	16.1/14.7/1.4	-0.83 ±0.17	6.1E-16/2.5E-16	S2458	0.34	16.20	15.28	15.33
53	2	18:43:22.82	-3 52 28.6	0.24	4.4/0.0/2.8	10.6/1.3/9.1	0.75 ±0.25	6.2E-18/4.5E-15	No	...	...	...	...
54	2	18:43:22.98	-3 57 53.0	0.19	7.5/7.7/0.0	17.8/16.8/0.9	-0.89 ±0.11	6.0E-16/2.4E-16	S2739/J18432299-0357526	0.47	13.92	13.48	13.25
55	2	18:43:23.03	-3 57 25.3	0.26	5.2/5.0/0.0	11.9/9.6/2.2	-0.63 ±0.27	3.0E-16/1.2E-15	S2749	0.66	17.00	15.77	15.17
56	2	18:43:23.30	-3 48 51.7	0.31	15.3/17.2/0.0	64.1/64.1/0.0	-1.00 ±0.03	2.9E-15/1.2E-15	S2844/J18432331-0348521	0.47	14.78	14.09	13.81
57	2	18:43:23.39	-3 58 05.1	0.21	9.6/10.9/0.0	27.1/25.3/1.9	-0.86 ±0.11	8.1E-16/3.3E-16	S2871/J18432340-0358050	0.19	13.26	12.23	11.82
58	2	18:43:23.62	-3 53 14.1	0.21	4.6/3.4/0.0	10.9/7.5/3.3	-0.39 ±0.30	2.5E-16/1.0E-15	S2932/J18432360-0353138	0.13	15.57	14.57	14.38
59	2	18:43:23.68	-3 51 40.6	0.23	6.6/6.0/0.0	14.4/13.4/1.0	-0.86 ±0.19	5.2E-16/2.1E-16	S2956	0.09	15.71	14.97	14.69
60	2	18:43:23.72	-4 00 26.0	0.42	8.5/5.4/3.1	40.9/28.4/11.4	-0.43 ±0.15	7.5E-16/3.1E-16	OoF	...	...	...	...
61	2	18:43:23.89	-3 53 31.4	0.18	5.4/2.8/4.6	17.4/6.2/10.8	0.27 ±0.25	1.1E-16/3.4E-15	No	...	...	...	...
62[T]	2	18:43:23.96	-3 57 58.9	0.18	13.2/10.7/5.2	39.0/27.0/12.0	-0.38 ±0.15	8.7E-16/3.6E-15	S3040	0.65	16.87	15.96	15.31
63	2	18:43:24.33	-4 03 38.5	1.09	0.0/4.3/0.0	21.5/21.5/0.0	-1.00 ±0.11	2.2E-16/8.7E-17	OoF	...	...	...	...
64	2	18:43:24.47	-3 53 49.8	0.06	42.1/39.3/9.0	101.2/84.3/16.7	-0.67 ±0.07	2.2E-15/9.1E-16	S3203/J18432446-0353495	0.05	13.72	12.64	12.21
65	2	18:43:24.81	-3 59 16.2	0.34	5.6/5.6/0.0	16.7/16.0/0.7	-0.91 ±0.12	5.8E-16/2.4E-16	S3312	0.47	16.37	15.36	14.77
66	2	18:43:25.04	-3 57 51.0	0.22	6.5/6.9/0.0	17.3/16.6/0.7	-0.92 ±0.12	6.2E-16/2.5E-16	S3394/J18432504-0357511	0.17	15.22	14.45	14.13
67	2	18:43:25.25	-3 59 15.3	0.30	6.6/6.4/0.0	23.6/18.3/5.3	-0.55 ±0.19	6.1E-16/2.5E-16	S3450/J18432523-0359150	0.55	15.96	15.23	14.88
68	2	18:43:26.14	-3 56 49.7	0.14	11.2/9.4/2.3	26.4/19.9/6.4	-0.51 ±0.18	7.1E-16/2.9E-16	S3833	0.42	16.51	15.61	15.21
69	2	18:43:26.41	-3 57 05.9	0.17	4.0/0.0/4.2	9.9/0.0/9.8	1.00 ±0.21	6.5E-16/4.7E-15	No	...	...	...	...
70	1	18:43:28.34	-4 07 33.2	0.31	21.3/25.4/0.0	175.1/169.0/6.0	-0.93 ±0.03	4.2E-15/1.7E-15	J18432835-0407331	0.26	9.06	8.79	8.54
71	2	18:43:28.35	-3 46 18.2	0.76	4.0/3.8/0.0	17.4/17.4/0.0	-1.00 ±0.13	6.6E-16/2.7E-16	OoF	...	...	...	...
72	2	18:43:28.67	-3 56 22.8	0.15	4.0/3.4/0.0	8.4/6.8/1.6	-0.62 ±0.30	1.8E-16/7.2E-16	S4885	0.27	17.29	14.81	14.70
73	2	18:43:28.91	-3 57 33.3	0.12	10.8/10.6/0.0	22.7/20.2/2.5	-0.78 ±0.14	5.1E-16/2.1E-15	S4992/J18432891-0357332	0.04	14.41	13.50	13.16
74	2	18:43:29.11	-3 59 42.3	0.39	4.3/0.0/2.5	14.8/5.4/9.3	0.26 ±0.27	8.2E-17/2.5E-15	S5111	0.69	17.85	15.39	15.76
75	2	18:43:29.26	-3 50 50.9	0.25	6.7/7.1/0.0	16.4/15.7/0.8	-0.90 ±0.12	4.7E-16/1.9E-16	S5148/J18432926-0350504	0.16	14.90	14.12	13.82
76	2	18:43:29.32	-3 56 48.7	0.15	8.9/0.0/9.3	22.1/0.5/21.5	0.95 ±0.09	1.5E-17/1.1E-14	No	...	...	...	...
77	1	18:43:29.33	-4 05 19.4	0.48	3.9/5.3/0.0	23.3/23.2/0.0	-1.00 ±0.11	9.2E-16/3.7E-16	J18432934-0405185	0.84	13.78	13.28	13.14
78	2	18:43:29.55	-3 46 56.5	0.52	3.8/0.0/4.0	18.4/0.7/17.7	0.93 ±0.12	1.1E-17/7.7E-15	OoF	...	...	...	...
79	2	18:43:29.70	-3 50 15.1	0.31	5.5/5.0/2.6	20.1/2.8/16.7	0.71 ±0.17	1.2E-17/8.4E-15	S5359	0.30	...	...	12.90
80	2	18:43:30.20	-3 51 18.2	0.21	4.5/4.0/0.0	9.2/7.8/1.4	-0.70 ±0.28	2.8E-16/1.1E-15	No	...	...	...	...
81	2	18:43:30.21	-3 53 44.3	0.17	4.2/4.7/0.0	9.9/9.5/0.5	-0.90 ±0.19	3.4E-16/1.4E-16	S5569/J18433019-0353440	0.33	15.37	14.73	14.50
82	2	18:43:30.27	-3 54 11.4	0.05	49.2/42.1/10.7	103.5/82.4/20.9	-0.60 ±0.08	3.7E-15/1.5E-14	S5602/J18433026-0354110	0.39	13.11	12.07	11.67
83	1/2	18:43:30.35	-3 59 43.3	0.43	0.0/5.0/0.0	15.8/15.8/0.0	-1.00 ±0.11	3.5E-16/1.4E-16	No	...	...	...	...
84[T]	1	18:43:30.52	-4 03 50.3	0.48	6.4/6.0/0.0	33.1/25.5/7.8	-0.53 ±0.17	7.3E-16/3.0E-15	No	...	...	...	...
85	2	18:43:30.63	-3 53 52.0	0.14	5.4/5.8/0.0	10.5/10.5/0.0	-1.00 ±0.18	3.5E-16/1.4E-16	S5758/J18433062-0353515	0.29	11.93	11.26	11.00
86[T]	1/2	18:43:30.75	-4 01 02.5	0.26	16.5/20.5/0.0	75.8/74.2/0.9	-0.97 ±0.03	2.2E-15/9.0E-16	S5825/J18433077-0401025	0.41	9.67[b]	9.40[b]	9.27[b]
87	1	18:43:30.80	-4 00 45.9	0.65	4.3/4.5/0.0	19.0/18.9/0.0	-1.00 ±0.13	5.6E-16/2.3E-16	S5840/J18433081-0400459	0.35	15.51	14.83	...
88	2	18:43:31.28	-3 50 29.1	0.23	12.6/2.8/9.3	37.7/11.8/25.1	0.36 ±0.16	2.4E-16/7.2E-15	No	...	...	...	...
89	2	18:43:31.30	-3 46 18.0	0.70	6.4/7.6/0.0	34.6/34.8/-0.0	-1.00 ±0.07	9.5E-16/3.8E-16	OoF	...	...	...	...
90	2	18:43:31.47	-3 55 15.8	0.23	4.9/2.9/0.0	10.0/5.6/4.5	-0.11 ±0.33	2.2E-16/7.6E-16	S6146	0.48	16.98	15.82	15.53
91	1/2	18:43:31.59	-3 56 49.4	0.11	14.9/14.0/2.4	32.0/25.9/6.0	-0.62 ±0.11	5.5E-16/2.3E-15	S6217/J18433157-0356492	0.18	14.23	13.53	13.30
92	2	18:43:31.68	-3 48 39.3	0.45	4.3/4.5/0.0	16.8/16.8/0.0	-1.00 ±0.13	5.3E-16/2.1E-16	S6289/J18433170-0348390	0.56	12.40	11.94	11.77
93	2	18:43:31.72	-3 59 56.1	0.48	4.0/0.0/2.7	10.9/5.7/5.2	-0.05 ±0.32	5.0E-17/1.5E-15	No	...	...	...	...
94	2	18:43:31.75	-3 51 26.7	0.15	10.7/9.3/1.9	26.1/19.9/6.1	-0.53 ±0.17	5.7E-16/2.4E-15	S6293/J18433170-0351268	0.55	15.21	14.20	13.41
95	2	18:43:31.76	-3 57 39.3	0.15	13.2/3.7/11.0	34.0/8.3/25.7	0.51 ±0.16	2.4E-16/7.1E-15	No	...	...	...	...
96	2	18:43:31.78	-3 57 17.2	0.20	4.3/3.8/0.0	9.5/7.9/1.6	-0.66 ±0.27	1.7E-16/6.9E-16	S6318	0.07	15.47	15.63	13.93
97	2	18:43:32.27	-3 54 44.7	0.16	6.9/6.2/0.0	16.0/14.6/1.5	-0.81 ±0.17	4.5E-16/1.8E-16	No	...	...	...	...
98	1/2	18:43:32.41	-4 00 50.4	0.39	5.2/5.7/0.0	14.0/12.9/1.2	-0.85 ±0.18	3.9E-16/1.6E-16	S6584/J18433236-0400507	0.70	15.78	15.04	...

Table 1—Continued

ID[a]	AO	R.A. (hh:mm:ss.ss) (J2000)	Dec. (d:mm:ss.s) (J2000)	Error (arcsec)	Significance (σ) Total/Soft/Hard	Normalized counts (cnts/100ks) Total/Soft/Hard	Hardness (H-S)/(H+S)	Flux (ergs s^{-1} cm^{-2}) 0.5-2keV/2-10keV	ID[b]	NIR counterpart separation (arcsec)	J[c] (mag)	H[c] (mag)	Ks[c] (mag)
99	1	18:43:32.47	-4 08 49.7	0.51	9.9/0.0/10.1	77.3/13.0/64.7	0.67 ±0.10	3.4E-17/2.5E-14	OoF	...	...	...	...
100	1	18:43:32.58	-4 04 18.7	0.21	31.3/19.7/23.9	222.8/99.3/125.0	0.11 ±0.07	1.6E-15/4.7E-14	J18433257-0404190	0.32	15.14	12.55	11.14
101	2	18:43:32.67	-3 49 07.6	0.37	4.5/0.3/5.1	16.0/0.0/15.7	1.00 ±0.14	8.1E-18/5.9E-15	No	...	...	...	...
102	2	18:43:33.36	-3 54 36.0	0.17	4.0/3.3/0.0	9.3/7.7/1.0	-0.66 ±0.27	2.4E-16/9.8E-16	S7035	0.05	16.53	15.47	15.01
103	2	18:43:33.41	-3 50 19.5	0.20	11.2/11.6/1.8	32.7/30.2/2.0	-0.84 ±0.10	7.0E-16/2.8E-16	S7055/J18433338-0350200	0.58	15.24	14.15	13.52
104	1	18:43:33.47	-4 03 54.3	0.51	3.6/4.5/0.0	25.2/17.5/7.8	-0.38 ±0.21	6.3E-16/2.6E-15	J18433350-0403541	0.52	11.62	10.71	10.35
105	2	18:43:33.94	-3 52 53.0	0.12	4.7/0.0/3.9	6.5/0.7/5.5	0.77 ±0.30	4.5E-18/3.3E-15	S7294/J18433392-0352529	0.08	...	14.89	13.09
106	2	18:43:34.12	-3 55 23.8	0.15	7.0/7.3/0.0	13.6/13.6/0.0	-1.00 ±0.15	2.8E-16/1.1E-16	S7436	0.45	15.25	14.47	14.10
107	2	18:43:34.13	-3 50 47.5	0.32	3.7/4.3/0.0	24.2/7.0/17.3	0.43 ±0.21	2.3E-16/9.3E-17	S7413	0.24	10.95	16.15	...
108	1	18:43:34.63	-4 10 32.2	0.92	3.8/0.0/5.0	9.0/8.2/0.8	-0.82 ±0.21	1.3E-16/3.8E-15	OoF	...	...	...	...
109	2	18:43:34.79	-3 40 04.2	0.70	4.4/4.6/0.0	28.5/26.8/1.7	-0.88 ±0.11	8.6E-16/3.5E-16	OoF	...	...	...	...
110	1/2	18:43:35.33	-4 00 44.7	0.35	7.1/7.4/0.0	20.3/16.7/3.7	-0.66 ±0.13	5.0E-16/2.1E-15	OoF	...	...	...	...
111	2	18:43:35.38	-3 55 56.6	0.13	4.1/4.4/0.0	8.5/8.7/0.3	-1.00 ±0.09	2.4E-16/9.6E-17	S8090/J18433529-0400448	0.48	15.01	14.66	14.44
112	2	18:43:35.41	-3 57 14.8	0.25	4.9/5.0/0.0	10.7/10.5/0.2	-0.96 ±0.19	2.5E-16/1.0E-16	S8139	0.32	10.63	10.96	14.93
113	1/2	18:43:35.45	-4 01 12.7	0.34	10.1/1.3/7.9	34.5/9.2/25.6	0.53 ±0.10	1.8E-16/5.4E-15	S8164	0.08	16.42	15.38	13.51
114	2	18:43:35.48	-3 58 46.1	0.29	4.6/3.1/3.3	17.3/9.3/8.0	-0.07 ±0.25	0.4E-17/1.9E-15	S8192	0.35	10.40	15.09	13.08
115	2	18:43:35.59	-3 40 00.8	0.58	6.2/6.0/0.0	60.7/51.5/9.3	-0.69 ±0.10	1.2E-16/5.0E-15	S8194/J18433545-0358456	0.27	14.74	14.01	...
116	2	18:43:35.82	-3 58 54.4	0.29	4.9/4.6/0.0	13.1/11.4/1.9	-0.72 ±0.20	1.5E-16/0.1E-16	OoF	...	...	...	...
117	2	18:43:35.84	-3 46 52.7	0.33	20.1/9.5/17.5	143.1/39.9/103.1	0.44 ±0.08	8.9E-16/2.7E-14	S8433/J18433584-0358539	0.68	14.35	13.66	13.34
118	2	18:43:35.89	-3 57 58.7	0.24	6.1/6.5/0.0	14.8/14.6/0.1	-0.99 ±0.14	2.5E-16/1.0E-16	OoF	...	...	...	...
119	1/2	18:43:36.18	-4 01 54.2	0.38	5.6/6.3/0.0	12.1/12.1/0.0	-1.00 ±0.16	4.2E-16/1.7E-16	S8464/J18433588-0357887	0.10	15.77	14.87	14.49
120	2	18:43:36.39	-3 55 50.1	0.13	5.1/0.6/6.0	9.6/0.0/1.5	1.00 ±0.21	5.9E-18/4.3E-15	S8621	0.94	16.09	15.59	...
121	2	18:43:36.43	-3 55 53.7	0.16	5.5/1.5/4.8	12.3/2.7/9.5	0.56 ±0.25	1.0E-16/4.8E-15	No	...	...	...	...
122	1/2	18:43:36.74	-3 57 47.9	0.21	7.6/7.8/0.0	21.8/19.1/2.0	-0.82 ±0.11	5.2E-16/2.1E-16	No	...	...	...	...
123	2	18:43:36.85	-3 54 29.4	0.19	0.6/6.9/0.0	14.5/14.3/0.3	-0.96 ±0.13	4.1E-16/1.7E-16	S8957/J18433676-0357478	0.32	15.52	14.71	14.38
124	1	18:43:37.01	-4 02 34.5	0.45	4.3/2.9/0.0	15.1/13.0/2.2	-0.71 ±0.21	1.9E-16/7.7E-16	S9010	0.27	16.65	15.09	16.12
125	2	18:43:37.07	-3 57 44.4	0.28	3.8/4.4/0.0	9.5/9.5/0.0	-1.00 ±0.21	3.1E-16/1.2E-16	No	...	...	...	...
126[T]	1	18:43:37.87	-4 03 53.2	0.25	16.6/4.7/14.6	75.7/21.8/55.1	0.43 ±0.11	5.8E-16/1.8E-14	S9480/J18433767-0357442	0.29	11.92	11.25	11.02
127	2	18:43:38.17	-4 09 46.9	0.37	10.8/12.3/0.0	51.1/48.9/2.3	-0.91 ±0.07	1.8E-15/7.1E-16	No	...	...	...	...
128	2	18:43:38.28	-3 52 01.1	0.18	9.6/9.7/0.0	9.6/9.7/0.0	-1.00 ±0.20	4.2E-16/1.7E-16	J18433817-0409465	0.39	14.43	12.65	11.81
129	1	18:43:38.59	-4 05 58.7	0.37	4.8/5.1/0.0	19.2/15.6/3.7	-0.62 ±0.22	5.5E-16/2.3E-15	S9809/J18433826-0352012	0.30	15.73	14.74	14.32
130	2	18:43:38.63	-3 57 32.7	0.19	7.9/7.9/0.0	19.0/17.7/1.3	-0.86 ±0.14	3.0E-16/1.2E-15	No	...	...	...	...
131[T]	2	18:43:38.73	-3 48 34.4	0.35	6.1/3.4/4.9	38.5/24.5/13.9	-0.28 ±0.16	5.7E-16/2.4E-15	No	...	...	...	...
132	2	18:43:39.02	-3 54 44.0	0.14	6.3/6.6/0.0	13.0/12.5/0.0	-0.91 ±0.14	3.6E-16/1.4E-16	S10021	0.38	16.06	15.13	14.84
133	2	18:43:39.04	-3 52 45.9	0.06	57.2/66.3/5.8	159.0/138.0/20.5	-0.74 ±0.05	2.9E-15/1.1E-15	S10209	...	...	...	...
134	2	18:43:39.04	-3 52 13.6	0.16	7.7/8.5/0.0	18.1/17.8/0.4	-0.96 ±0.11	0.9E-16/2.8E-16	S10275/J18433902-0352459	0.19	13.16	17.09	11.88
135	2	18:43:39.28	-3 52 52.5	0.14	12.0/13.../0.0	28.6/28.6/0.2	-0.99 ±0.07	9.7E-16/3.9E-16	S10271/J18433901-0352138	0.25	12.51	12.21	11.88
136	1	18:43:39.26	-4 07 02.5	0.46	4.7/0.0/3.8	16.0/2.5/14.1	0.70 ±0.22	1.0E-17/7.5E-15	S10406/J18433923-0352523	0.45	10.38	12.01	9.85[b]
137	2	18:43:39.38	-3 49 53.7	0.17	30.1/2.1/34.0	140.5/7.8/135.7	0.89 ±0.04	7.3E-17/5.3E-14	No	0.41	...	10.21	...
138	1	18:43:39.51	-4 05 14.2	0.22	15.8/2.0/15.7	62.0/9.4/52.8	0.70 ±0.10	3.6E-17/2.6E-14	No	...	...	...	...
139	2	18:43:39.76	-3 54 08.8	0.15	20.6/19.4/1.3	20.6/19.4/1.3	-0.87 ±0.12	6.3E-16/2.5E-16	S10699	...	...	...	...
140	2	18:43:40.34	-3 51 54.3	0.22	4.7/4.6/0.0	12.9/10.7/2.3	-0.65 ±0.24	2.8E-16/1.1E-15	S11045/J18434031-0351544	0.42	16.24	15.36	15.04
141	1	18:43:40.60	-4 03 42.1	0.36	6.8/8.2/1.3	20.4/13.8/3.8	-0.34 ±0.23	3.2E-16/1.3E-15	No	0.11	14.41	14.60	14.36
142	2	18:43:40.95	-3 49 54.9	0.42	2.7/4.1/0.0	10.9/10.9/0.1	-0.98 ±0.19	2.8E-16/1.2E-16	No	...	...	...	...
143[T]	1/2	18:43:41.02	-3 58 02.3	0.32	3.9/4.3/0.0	10.8/14.2/2.6	-0.80 ±0.18	3.7E-16/1.5E-15	No	...	...	...	...
144	1/2	18:43:41.13	-3 57 40.6	0.11	36.9/32.7/9.4	62.4/55.2/7.8	-0.73 ±0.08	1.6E-15/6.6E-15	S11475/J18434103-0358024	0.27	12.20	11.18	10.73
145	2	18:43:41.51	-3 50 55.0	0.27	4.5/0.0/2.5	11.4/5.3/6.1	0.07 ±0.32	9.7E-17/2.9E-15	S11523/J18434111-0357404	0.19	12.92	12.10	11.77
146	1	18:43:41.81	-4 11 18.6	0.53	4.0/0.0/5.1	16.7/0.0/13.9	1.00 ±0.15	1.1E-17/7.9E-15	OoF	...	...	...	...
147	2	18:43:42.17	-3 57 59.0	0.22	6.3/6.2/0.0	16.9/14.8/1.2	-0.85 ±0.17	2.7E-16/1.1E-16	S12123	0.40	15.35	14.59	14.30

Table 1—Continued

ID[a]	AO	R.A. (hh:mm:ss.ss) (J2000)	Dec. (d:mm:ss.s)	Error (arcsec)	Significance (σ) Total/Soft/Hard	Normalized counts (cnts/100ks) Total/Soft/Hard	Hardness (H-S)/(H+S)	Flux (ergs s^{-1} cm^{-2}) 0.5-2keV/2-10keV	ID[b]	NIR counterpart separation (arcsec)	J[c] (mag)	H[c] (mag)	Ks[c] (mag)
148	2	18:43:42.37	-3 55 07.4	0.15	6.0/5.9/0.0	12.1/11.6/0.6	-0.91 ±0.15	3.4E-16/1.4E-16	S12222	0.24	17.84	16.60	16.11
149	1/2	18:43:42.57	-3 59 41.1	0.26	6.0/5.8/0.0	18.0/11.8/6.2	-0.32 ±0.17	4.0E-16/1.6E-15	S12331	0.70	15.46	14.64	14.45
150	2	18:43:42.73	-3 54 24.7	0.16	9.3/8.7/0.0	22.5/18.3/4.0	-0.64 ±0.17	5.1E-16/2.1E-15	S12469	0.21	17.76	15.88	15.61
151	2	18:43:43.26	-3 51 56.9	0.22	12.6/0.0/13.3	47.9/5.1/41.7	0.78 ±0.10	2.6E-17/1.9E-14	No	...	...	...	...
152	1	18:43:43.42	-4 04 51.1	0.27	3.7/4.1/0.0	9.9/9.9/0.0	-1.00 ±0.23	3.6E-16/1.5E-16	No	...	...	...	...
153	2	18:43:43.80	-3 47 33.2	0.48	6.7/7.1/0.0	44.6/36.6/6.9	-0.68 ±0.12	1.0E-15/4.2E-15	OoF	...	...	...	...
154	1	18:43:45.01	-4 03 34.5	0.26	4.8/4.6/0.0	11.9/10.6/1.4	-0.77 ±0.25	4.8E-16/2.0E-16	S14192	0.65	...	15.87	13.11
155	1	18:43:45.04	-4 05 01.6	0.16	17.2/17.6/2.7	52.9/44.8/8.1	-0.69 ±0.11	1.1E-15/4.5E-15	S14243/J18434503-0405015	0.17	14.67	13.54	13.75
156	2	18:43:45.35	-3 53 16.7	0.25	4.6/3.8/0.0	17.0/11.2/5.8	-0.32 ±0.24	3.9E-16/1.6E-15	S14512/J18434537-0353163	0.60	15.33	14.02	...
157	1	18:43:45.87	-4 07 39.6	0.32	4.5/5.1/0.0	14.1/13.4/0.7	-0.90 ±0.16	2.2E-16/8.7E-17	S14852/J18434586-0407387	0.83	15.75	14.44	14.44
158	2	18:43:46.06	-3 53 51.8	0.17	5.7/6.6/0.0	16.0/15.7/0.4	-0.95 ±0.12	4.5E-16/1.8E-16	S15011/J18434607-0353521	0.12	14.51	14.74	14.44
159	1	18:43:46.08	-4 03 24.6	0.21	4.0/4.6/0.0	8.6/8.6/0.0	-1.00 ±0.26	2.2E-16/9.0E-17	S15029/J18434610-0403248	0.38	14.07	13.91	13.63
160	1	18:43:46.08	-4 05 48.7	0.23	5.8/6.2/0.0	15.5/15.2/0.3	-0.96 ±0.14	4.7E-16/1.9E-16	S15003/J18434605-0405488	0.49	14.21	13.30	13.04
161	2	18:43:46.43	-3 54 11.6	0.23	5.1/6.2/0.0	13.3/13.4/0.0	-1.00 ±0.15	4.9E-16/2.0E-16	S15282/J18434644-0354117	0.33	...	13.53	13.36
162	1	18:43:46.62	-4 04 30.1	0.11	22.9/0.0/25.3	67.8/1.4/66.4	0.96 ±0.05	3.8E-17/2.8E-14	No	...	...	...	...
163	2	18:43:46.66	-3 46 23.8	0.78	3.8/5.6/0.0	24.8/24.7/0.0	-1.00 ±0.09	8.8E-16/3.6E-16	OoF	...	...	...	...
164	2	18:43:46.72	-3 54 43.5	0.21	4.5/3.7/0.0	10.1/7.6/2.5	-0.51 ±0.29	2.0E-16/8.1E-16	S15492/J18434671-0354434	0.06	15.42	14.14	13.38
165[T]	1	18:43:46.79	-4 07 06.3	0.29	7.9/6.9/0.0	21.8/16.7/5.1	-0.53 ±0.20	4.6E-16/1.9E-15	No	...	...	...	...
166[T]	1	18:43:46.81	-4 01 25.7	0.18	12.2/12.8/0.0	37.0/33.5/3.5	-0.81 ±0.12	6.5E-16/2.7E-16	S15573/J18434683-0401264	0.83	12.20	11.32	11.05
167	1	18:43:46.96	-4 10 32.7	0.31	9.3/8.8/3.0	37.6/30.3/7.3	-0.61 ±0.15	8.9E-16/3.7E-15	S15657/J18434694-0410326	0.36	14.90	13.81	13.41
168	1	18:43:47.10	-4 08 40.6	0.37	5.8/4.2/0.0	17.8/10.7/7.0	-0.21 ±0.26	1.9E-16/7.7E-16	No	...	...	...	...
169	2	18:43:47.11	-3 53 18.3	0.18	10.3/9.8/0.0	28.3/22.4/5.9	-0.58 ±0.15	7.0E-16/2.9E-15	S15778/J18434709-0353182	0.11	15.65	14.60	14.23
170	1	18:43:47.37	-4 08 30.4	0.17	23.7/27.2/0.0	89.8/89.7/0.2	-0.99 ±0.03	2.3E-15/9.5E-16	S15972/J18434736-0408301	0.32	...	12.36	12.23
171[T]	1	18:43:47.55	-4 04 06.1	0.19	5.2/3.8/1.5	13.8/8.5/5.2	-0.24 ±0.29	2.9E-16/1.2E-15	No	...	...	...	...
172	1/2	18:43:47.63	-3 56 10.3	0.18	13.5/14.4/0.0	46.1/33.7/12.3	-0.44 ±0.12	9.6E-16/3.9E-15	S16177/J18434762-0356105	0.20	15.70	14.84	14.66
173	1/2	18:43:47.79	-3 59 19.0	0.29	6.1/0.0/6.5	18.3/1.3/16.4	0.85 ±0.12	1.1E-17/8.2E-15	No	...	...	...	...
174	2	18:43:48.04	-3 53 57.5	0.26	6.0/0.0/6.8	22.3/2.7/19.3	0.76 ±0.15	1.3E-17/9.3E-15	No	...	...	...	...
175	1	18:43:48.08	-4 03 03.4	0.28	4.4/0.0/4.2	10.9/1.6/9.2	0.71 ±0.27	5.5E-18/4.0E-15	No	...	...	...	...
176	1	18:43:48.67	-4 01 36.1	0.10	37.6/40.3/4.7	134.8/122.4/12.4	-0.82 ±0.05	1.7E-15/6.8E-16	S16952/J18434867-0401362	0.13	14.42	13.61	13.37
177[T]	1	18:43:48.72	-4 01 17.6	0.32	4.5/3.1/0.0	16.8/10.2/6.5	-0.22 ±0.26	1.2E-16/5.0E-16	No	...	...	...	...
178	1/2	18:43:49.03	-3 59 57.1	0.24	7.4/7.1/4.7	30.6/17.9/12.6	-0.35 ±0.12	4.4E-16/1.8E-15	S17276	0.92	16.55	14.65	13.68
179	1	18:43:49.11	-4 02 56.4	0.18	4.3/4.2/0.0	10.4/8.5/1.8	-0.66 ±0.27	3.5E-16/1.4E-15	S17301	0.22	16.95	15.48	14.93
180	1	18:43:49.21	-4 00 54.1	0.30	5.4/2.5/3.8	14.2/4.4/9.8	0.39 ±0.27	5.0E-17/1.5E-15	No	...	...	...	...
181[T]	2	18:43:49.22	-3 52 38.3	0.22	15.2/14.2/3.7	61.8/46.1/15.8	-0.49 ±0.11	1.2E-15/4.9E-15	S17370	0.46	16.88	16.10	15.67
182	1	18:43:49.39	-4 04 13.7	0.18	8.5/4.2/5.1	21.1/9.5/11.7	0.11 ±0.24	1.7E-16/5.1E-15	No	...	...	...	...
183	1	18:43:50.42	-4 02 29.5	0.17	4.0/4.3/0.0	9.7/9.7/0.0	-1.00 ±0.22	2.5E-16/1.0E-16	No	...	...	...	...
184	1	18:43:50.51	-4 02 07.2	0.17	4.7/4.1/0.0	11.5/9.8/1.9	-0.68 ±0.24	3.1E-16/1.3E-15	S18344/J18435042-0402294	0.11	13.87	13.21	12.95
185	1/2	18:43:50.67	-3 58 52.1	0.31	2.7/4.0/0.0	7.9/7.2/0.6	-0.84 ±0.24	2.6E-16/1.1E-16	S18402	0.19	16.71	15.36	14.93
186	1/2	18:43:50.71	-3 57 38.8	0.33	7.0/0.0/7.3	33.9/6.9/27.0	0.65 ±0.10	1.9E-16/1.4E-14	S18522/J18435067-0358526	0.62	14.97	14.37	14.13
187	2	18:43:51.09	-3 52 39.1	0.18	21.4/25.0/0.0	82.9/82.0/0.9	-0.98 ±0.02	2.4E-15/9.8E-16	S18799	0.29	...	10.90	...
188	1/2	18:43:51.81	-3 59 22.3	0.21	13.6/12.6/2.2	38.0/30.8/7.2	-0.62 ±0.10	9.2E-16/3.8E-15	S19355/J18435181-0359222	0.03	14.93	14.01	13.54
189	1	18:43:52.37	-4 07 29.9	0.20	7.4/6.8/0.0	19.0/16.3/2.7	-0.71 ±0.19	5.1E-16/2.1E-16	No	...	...	...	...
190	2	18:43:52.78	-3 53 59.3	0.35	5.8/4.0/0.0	23.0/18.4/4.6	-0.60 ±0.18	4.4E-16/1.8E-15	No	...	...	...	...
191	1/2	18:43:52.78	-4 00 50.1	0.24	7.9/8.6/0.0	24.4/20.1/4.8	-0.49 ±0.13	5.0E-16/2.0E-15	S20105	0.67	16.39	15.19	14.62
192	1	18:43:52.85	-3 57 59.8	0.21	4.4/2.4/0.0	10.1/8.4/1.7	-0.66 ±0.28	3.1E-16/1.3E-15	No	...	...	...	...
193	1/2	18:43:53.11	-3 51 16.3	0.30	5.5/7.2/0.0	25.0/19.1/6.0	-0.57 ±0.14	5.3E-16/2.2E-15	S20390/J18435312-0357594	0.48	13.47	12.93	12.71
194	2	18:43:53.58	-3 55 16.3	0.42	5.0/6.8/0.0	33.9/26.4/7.6	-0.55 ±0.16	8.9E-16/3.7E-15	No	...	...	...	...
195	1/2	18:43:54.18	-3 58 44.0	0.43	0.0/4.9/0.0	14.4/10.2/4.2	-0.59 ±0.18	2.8E-16/1.2E-15	S21144	0.37	16.28	15.41	15.09
196	1/2	18:43:54.56	-3 58 06.3	0.34	6.2/6.2/0.0	39.7/28.0/11.7	-0.41 ±0.11	6.4E-16/2.7E-15	No	...	...	...	...

Table 1— Continued

ID[a]	AO	R.A. (hh:mm:ss.ss) (J2000)	Dec. (d:mm:ss.s)	Error (arcsec)	Significance (σ) Total/Sft/Hard	Normalized counts (cnts/100ks) Total/Soft/Hard	Hardness (H-S)/(H+S)	Flux (ergs s⁻¹ cm⁻²) 0.5-2keV/2-10keV	NIR counterpart ID[b]	separation (arcsec)	J[c] (mag)	H[c] (mag)	K_S[c] (mag)
197	1/2	18:43:54.61	−3 56 41.5	0.27	14.0/9.9/5.7	80.5/37.6/42.3	0.07 ±0.08	5.2E-16/1.6E-14	No	...	...	...	...
198	2	18:43:54.65	−3 53 36.5	0.43	5.3/5.6/0.0	20.9/18.3/2.4	−0.77 ±0.16	6.0E-16/2.5E-15	S21470/J18435406-0353364	0.34	15.67	14.70	14.23
199	1	18:43:54.83	−4 07 42.0	0.14	22.0/24.4/0.0	77.8/73.4/4.5	−0.88 ±0.06	1.9E-15/7.6E-16	S21560	0.42	14.31	13.57	13.32
200	1/2	18:43:55.10	−3 58 29.6	0.11	90.8/23.3/91.4	577.7/73.8/501.4	0.74 ±0.02	2.3E-16/1.7E-13	No	...	...	...	...
201	1	18:43:55.15	−4 04 20.1	0.15	7.2/7.0/0.0	15.1/15.1/0.0	−1.00 ±0.15	5.0E-16/2.0E-16	S21808	0.36	13.04	13.42	12.04
202	2	18:43:55.42	−3 52 52.9	0.21	21.7/18.8/11.8	98.7/55.3/42.4	−0.13 ±0.10	8.0E-16/2.4E-14	No	...	...	...	...
203	2	18:43:55.69	−3 57 04.3	0.49	4.3/0.3/5.0	25.6/2.5, 22.9	0.80 ±0.14	1.2E-17/8.7E-15	S22226	0.39	18.57	17.23	...
204	2	18:43:55.70	−3 52 50.2	0.30	10.1/0.0/8.0	45.6/18.2/26.4	0.18 ±0.15	3.7E-16/1.1E-14	S22272	0.93	17.37	16.05	15.34
205	1	18:43:55.78	−4 08 26.8	0.29	5.2/6.7/0.0	18.9/10.1/2.0	−0.78 ±0.16	4.0E-16/1.6E-16	No	...	...	...	...
206	1	18:43:55.90	−3 55 03.9	0.40	4.4/3.1/0.0	39.2/28.8/10.4	−0.47 ±0.15	5.8E-16/2.4E-15	No	...	...	...	...
207	1	18:43:56.08	−4 06 08.0	0.13	7.2/0.0/6.3	11.6/0.9/10.7	0.86 ±0.18	7.5E-18/5.4E-15	No	...	...	...	...
208[E]	2	18:43:56.68	−3 54 47.8	0.25	16.8/17.4/3.1	238.3/197.7/40.6	−0.66 ±0.05	2.7E-15/1.1E-14	No	...	...	...	...
209	1/2	18:43:56.90	−3 57 33.5	0.37	5.6/7.4/0.0	18.2/18.2/0.0	−1.00 ±0.10	5.5E-16/2.2E-16	No	...	...	...	...
210[E]	2	18:43:56.90	−3 54 37.0	0.30	8.4/0.0/0.0	125.1/86.8/38.4	−0.39 ±0.09	1.0E-15/6.5E-15	No	...	...	...	...
211	1	18:43:57.35	−4 01 23.3	0.21	5.5/2.4/2.8	14.3/4.9/9.2	0.30 ±0.28	1.2E-16/3.5E-15	No	...	...	...	...
212	2	18:43:57.68	−3 51 57.1	0.53	5.3/4.../0.0	29.9/17.1/12.9	−0.14 ±0.19	2.0E-16/6.0E-15	S23609	0.90	16.90	15.44	14.77.
213[E]	2	18:43:57.87	−3 54 45.9	0.31	0.4/0.0/4.2	188.3/126.3/61.1	−0.35 ±0.07	1.8E-15/7.4E-15	No	...	...	...	...
214	2	18:43:57.87	−4 07 37.7	0.10	23.3/24.6/0.0	60.5/58.9/1.6	−0.95 ±0.05	2.7E-15/1.1E-16	S23783/J18435787-0407379	0.37	12.82	12.12	11.95
215	1/2	18:43:57.91	−3 59 19.8	0.34	7.4/3.0/4.9	12.4/6.3/6.2	0.00 ±0.23	1.2E-16/3.7E-15	No	...	...	...	...
216[E]	2	18:43:57.92	−3 54 37.5	0.34	8.5/5.4/0.0	123.9/93.1/30.7	−0.50 ±0.08	1.4E-15/5.9E-15	No	...	...	...	...
217	1	18:43:58.30	−4 03 21.2	0.16	4.5/3.9/0.0	10.3/8.4/1.8	−0.65 ±0.26	2.6E-16/1.1E-15	S24066	0.36	16.81	15.44	14.80*
218	1/2	18:43:58.53	−3 56 21.6	0.31	9.4/2.1/9.0	36.8/8.6/28.3	0.53 ±0.12	2.4E-16/7.3E-15	No	...	...	...	...
219	2	18:43:59.02	−3 51 15.7	0.55	0.7/7.2/1.7	26.5/26.2/0.2	−0.98 ±0.08	1.0E-15/4.1E-16	No	...	...	...	...
220	2	18:43:59.28	−3 50 26.2	0.81	4.4/5.1/0.0	36.2/30.7/6.7	−0.64 ±0.13	8.7E-16/3.6E-15	OoI[F]	...	...	...	...
221	2	18:43:59.67	−3 55 18.3	0.41	10.0/10.5/0.0	59.0/55.4/4.3	−0.80 ±0.08	1.7E-15/0.8E-16	S25062/J18435905-0355183	0.21	9.30[b]	8.93[b]	8.70[b]
222	1	18:43:59.92	−4 07 21.5	0.23	5.2/2.4/0.0	11.9/8.2/3.6	−0.39 ±0.30	2.4E-16/1.0E-15	No	...	...	...	...
223	1	18:44:00.31	−4 05 59.2	0.13	8.4/7.6/0.0	19.8/17.1/2.7	−0.73 ±0.17	5.0E-16/2.0E-15	No	...	...	...	...
224[T]	1	18:44:01.13	−3 57 40.7	0.55	5.8/5.4/0.0	24.1/21.3/2.9	−0.76 ±0.16	2.7E-16/1.1E-15	S25554/J18440036-0405594	0.81	13.59	12.37	11.91
225	1	18:44:01.93	−4 05 11.7	0.19	4.4/3.4/0.0	10.1/7.2/2.7	−0.46 ±0.31	2.1E-16/8.5E-16	S26060	0.61	16.59	15.38	14.74
226	1	18:44:02.16	−4 05 23.7	0.11	20.8/22.4/0.0	56.2/56.3/0.4	−0.99 ±0.04	1.7E-15/6.8E-16	S26833/J18440213-0405243	0.93	14.18	13.41	13.15
227	2	18:44:02.44	−4 12 44.8	0.89	4.7/0.0/4.8	19.1/0.0/9.3	1.00 ±0.13	5.6E-16/4.0E-15	OoI[F]	...	...	...	...
228	2	18:44:02.45	−3 51 51.7	0.08	4.0/3.5/0.0	26.7/16.8/10.0	−0.25 ±0.20	4.5E-16/1.8E-15	No	...	...	...	...
229	1	18:44:02.54	−4 09 22.3	0.19	18.5/2.0/19.3	77.2/10.8/65.0	0.72 ±0.09	4.0E-17/2.9E-14	S27070/J18440256-0409228	0.38	13.15	13.67	12.20
230	1/2	18:44:03.27	−3 58 50.0	0.27	21.0/23.4/0.0	60.3/66.0/0.2	−0.99 ±0.03	1.9E-15/7.8E-16	S27370/J18440331-0358188	0.63	...	12.48	12.23
231	1	18:44:03.47	−4 10 41.8	0.50	5.8/2.4/3.2	25.5/17.6/7.8	−0.39 ±0.20	2.8E-16/1.2E-15	No	...	...	...	...
232[T]	1	18:44:03.84	−4 11 23.6	0.70	4.2/0.0/4.4	23.2/7.6/5.5	0.34 ±0.22	1.8E-15/6.4E-15	OoI[F]	...	...	...	...
233[T]	1	18:44:03.95	−4 02 57.6	0.10	31.2/11.8/24.4	90.3/29.3/57.5	0.32 ±0.11	6.3E-16/1.9E-14	S27641/J18440392-0402577	0.43	...	14.22	13.40
234	2	18:44:03.97	−3 54 06.6	0.73	5.8/6.1/4.7	44.2/24.3/19.9	−0.10 ±0.16	2.8E-16/8.3E-15	OoI[F]	...	...	...	...
235[T]	1	18:44:05.05	−4 04 36.9	0.10	26.2/13.1/15.0	04.9/31.0/32.7	0.03 ±0.13	6.7E-16/2.0E-14	S28081	0.80	17.40	15.35	...
236	1	18:44:05.41	−4 08 32.4	0.14	24.5/25.4/0.0	89.4/84.5/5.0	−0.89 ±0.05	2.3E-15/9.3E-16	S28203/J18440540-0408325	0.17	14.98	14.31	14.07
237	1	18:44:05.56	−4 05 39.1	0.19	6.4/4.8/0.0	15.1/10.4/4.6	−0.39 ±0.26	3.8E-16/1.6E-15	S28248	0.52	16.59	15.28	14.87
238	1	18:44:05.91	−4 06 12.2	0.10	21.0/18.3/3.9	51.6/42.5/9.0	−0.65 ±0.15	1.1E-15/4.0E-15	S28382/J18440589-0406124	0.53	14.27	13.36	13.10
239	1	18:44:06.10	−4 08 43.5	0.22	5.7/6.3/0.0	19.7/18.4/1.3	−0.87 ±0.15	5.2E-16/2.1E-16	No	...	...	...	...
240	1	18:44:06.35	−4 07 04.0	0.20	5.6/0.0/5.6	13.0/0.8/12.5	0.88 ±0.16	8.4E-18/6.1E-15	No	...	...	...	...
241	1	18:44:07.60	−4 05 14.1	0.17	8.5/0.0/6.7	21.7/2.8/18.3	0.74 ±0.17	1.2E-17/8.4E-15	No	...	...	...	...
242	2	18:44:08.59	−3 53 55.8	0.68	6.2/0.0/6.8	53.2/4.5/49.7	0.84 ±0.09	3.0E-17/2.2E-14	OoI[F]	...	...	...	...
243	1	18:44:09.49	−4 07 31.6	0.17	12.8/0.0/11.8	41.0/2.0/37.0	0.90 ±0.08	2.4E-17/1.8E-14	No	...	...	...	...
244	1	18:44:10.98	−4 05 10.8	0.14	12.0/4.3/9.3	30.8/10.5/20.1	0.31 ±0.19	2.4E-16/7.1E-15	S30315/J18441095-0405170	0.51	15.60	13.55	12.71
245	1	18:44:11.89	−4 05 12.6	0.18	14.1/10.9/13.1	40.3/7.9/31.9	0.60 ±0.14	2.3E-17/1.7E-14	No	...	...	...	...

Table 1—Continued

ID[a]	AO	R.A. (hh:mm:ss.ss) (J2000)	Dec. (d:mm:ss.s)	Error (arcsec)	Significance (σ) Total/Soft/Hard	Normalized counts (cnts/100ks) Total/Soft/Hard	Hardness (H-S)/(H+S)	Flux (ergs s^{-1} cm^{-2}) 0.5-2keV/2-10keV	ID[b]	NIR conterpart separation (arcsec)	J[c] (mag)	H[c] (mag)	Ks[c] (mag)
246	1	18:44:11.90	−4 06 30.7	0.23	7.3/4.7/2.3	20.3/14.7/5.6	−0.45 ±0.22	5.9E-16/2.4E-15	S30539/J18441188-0406311	0.55	...	15.35	13.97
247	1	18:44:12.17	−4 08 08.2	0.32	2.3/0.0/4.1	13.0/2.5/10.2	0.61 ±0.27	8.7E-18/6.3E-15	No	...	...	...	...
248	1	18:44:13.16	−4 06 20.2	0.25	5.4/0.0/4.1	15.2/0.3/13.5	0.95 ±0.16	9.1E-18/6.6E-15	No	...	...	...	...
249[T]	1	18:44:13.72	−4 02 32.8	0.29	4.0/2.6/0.0	11.5/8.2/3.3	−0.42 ±0.32	2.8E-16/1.1E-15	No	...	...	...	...
250	1	18:44:13.77	−4 12 17.4	0.53	12.9/0.0/14.9	106.2/9.5/97.9	0.82 ±0.06	6.3E-17/4.6E-14	OoF	...	...	...	...
251	1	18:44:14.75	−4 12 34.7	0.44	11.0/11.0/2.0	64.3/50.6/13.7	−0.57 ±0.12	1.4E-15/5.9E-15	OoF	...	...	...	...
252	1	18:44:15.62	−4 03 56.9	0.31	6.5/2.8/4.0	22.0/9.4/12.4	0.14 ±0.24	1.6E-16/4.9E-15	S31107/J18441558-0403569	0.55	16.96	14.59	13.60
253	1	18:44:15.73	−4 08 58.0	0.49	4.6/0.0/4.2	18.3/5.8/12.4	0.36 ±0.25	1.7E-16/5.1E-15	No	...	...	...	...
254	1	18:44:16.25	−4 12 57.0	0.82	5.7/0.0/3.5	40.4/7.7/33.4	0.62 ±0.14	2.4E-17/1.7E-14	OoF	...	...	...	...
255	1	18:44:18.54	−4 06 02.5	0.29	8.3/6.2/3.9	37.1/27.2/9.8	−0.47 ±0.16	8.8E-16/3.6E-15	S31539/J18441855-0406027	0.35	13.54	12.59	12.11
256	1	18:44:21.13	−3 57 06.3	0.33	26.1/25.6/10.6	312.3/244.1/66.3	−0.57 ±0.05	5.4E-15/2.2E-14	OoF	...	...	15.35	14.57
257	1	18:44:21.60	−4 04 53.2	0.40	5.5/3.7/3.3	29.1/14.0/15.0	0.03 ±0.21	3.3E-16/1.0E-14	S31826	0.25	...	15.35	14.57
258	1	18:44:21.77	−4 12 30.1	0.48	14.5/12.7/6.7	179.3/124.8/55.4	−0.39 ±0.08	3.1E-15/1.3E-14	OoF	...	...	...	...
259	1	18:44:22.57	−3 59 39.8	0.57	6.1/7.2/0.0	55.6/39.1/16.5	−0.40 ±0.14	9.8E-16/4.0E-15	OoF	...	...	...	...
260[T]	1	18:44:22.61	−4 03 51.0	0.35	11.8/12.4/0.0	65.3/57.5/7.7	−0.76 ±0.09	1.5E-15/6.2E-15	S31912/J18442259-0403518	0.85	14.80	13.52	13.57
261	1	18:44:22.63	−4 00 40.0	0.50	6.7/0.0/8.2	42.8/0.0/42.9	1.00 ±0.06	2.7E-17/1.9E-14	OoF	...	...	...	...
262	1	18:44:22.67	−4 00 17.4	0.50	6.7/6.5/0.0	43.3/33.5/9.8	−0.55 ±0.15	7.0E-16/2.9E-15	J18442265-0400176	0.30	14.36	13.39	12.52
263	1	18:44:23.45	−4 03 08.5	0.50	5.1/0.0/3.3	23.8/3.7/20.0	0.69 ±0.18	1.1E-17/8.2E-15	No	...	...	...	...
264	1	18:44:24.09	−3 59 11.9	0.57	11.6/11.7/3.6	95.2/75.6/19.8	−0.59 ±0.09	1.8E-15/7.5E-15	J18442406-0359111	0.86	13.59	12.69	12.37
265	1	18:44:24.24	−4 01 35.1	0.52	5.4/5.2/0.0	28.3/24.0/4.2	−0.70 ±0.16	7.7E-16/3.2E-15	J18442423-0401343	0.72	16.00	14.70	13.83
266	1	18:44:26.23	−3 57 48.8	0.54	11.8/13.9/0.0	118.7/118.4/0.0	−1.00 ±0.02	2.7E-15/1.1E-15	OoF	...	...	...	...
267	1	18:44:26.45	−4 06 35.5	0.47	5.7/4.7/0.0	28.3/20.8/7.6	−0.47 ±0.19	5.1E-16/2.1E-15	No	...	...	14.58	...
268	1	18:44:26.66	−4 04 50.1	0.53	4.1/3.5/0.0	15.0/13.1/2.1	−0.73 ±0.21	3.0E-16/1.2E-15	S32241	0.80	15.61	14.58	14.12
269	1	18:44:26.71	−4 03 27.3	0.46	9.8/10.5/0.0	61.5/53.8/7.6	−0.75 ±0.10	1.2E-15/4.8E-15	No	...	...	...	...
270	1	18:44:27.75	−4 07 49.3	0.55	4.3/4.0/0.0	30.1/24.8/5.2	−0.65 ±0.16	8.2E-16/3.4E-15	OoF	...	...	...	...
271	1	18:44:28.51	−4 08 15.3	0.63	6.2/3.8/4.1	36.3/14.3/22.2	0.22 ±0.18	2.9E-16/8.8E-15	OoF	...	...	...	...
272	1	18:44:28.87	−4 01 03.9	0.48	14.3/12.1/8.3	142.0/85.8/57.2	−0.20 ±0.09	8.2E-16/2.5E-14	J18442884-0401033	0.60	13.29	11.83	11.11
273	1	18:44:30.35	−4 10 44.5	0.50	16.6/7.9/15.6	164.6/33.8/134.5	0.60 ±0.07	9.4E-17/6.8E-14	J18443035-0410445	0.12	17.37	15.68	13.90
274	1	18:44:32.73	−4 07 04.4	0.58	9.2/9.8/0.0	55.9/55.7/0.0	−1.00 ±0.05	1.9E-15/7.6E-16	OoF	...	...	...	...

[a] Sources with T in the ID column show significant time variations, and those with E are extended.

[b] SOFI ID in Table 1 (starts with S) and/or 2MASS ID (starts with J) of the NIR source within 1″ from the Chandra position. "No" means that the source is in the SOFI field of view, but there are no SOFI counterparts. "OoF" means that the source is out of the SOFI field, and no 2MASS counterparts.

[c] 2MASS magnitudes are taken for stars brighter than 10 mag, since SOFI starts to saturate for < 10 mag (see Fig. 5).

Table 2. SOFI NIR source catalog.

ID	R.A. (J2000)	Decl. (J2000)	J (mag)	H (mag)	K_S (mag)	2MASS ID	Chandra ID
1	18:43:08.380	−03:54:34.12	-999	17.64	15.58	...	...
2	18:43:08.382	−03:52:29.29	16.69	15.33	15.09	...	...
3	18:43:08.382	−03:53:46.51	17.37	16.56	16.40	...	...
...							
8	18:43:08.451	−03:54:07.29	-999	16.04	14.56	18430845−0354075	...
...							
687	18:43:15.299	−03:54:19.16	10.45	10.15	10.03	18431530−0354190	24
...							
1018	18:43:17.438	−03:57:32.71	16.54	15.25	15.13	...	30
...							
32397	18:44:28.474	−04:06:50.97	15.72	13.80	12.64	...	...
32398	18:44:28.477	−04:04:33.27	-999	-999	15.18	...	...

Note. — We have detected 32,398 sources from our SOFI fields (Fig. 3). For each source, the position, J, H and K_S magnitudes, and the 2MASS and/or *Chandra* counterparts are given. When not detected, −999 is put for the magnitude. The *Chandra* source identification number is defined in Table 1. The complete version of this table is in the electronic edition of the Journal. The printed edition contains only a sample.

Table 3. Summary of the point source characteristics.

hardness ratio	soft ≤ -0.60	Medium -0.59 to 0.1	Hard ≥ 0.11	Total
All	137	68	69	274
Extended[a]	1	3	0	4
Point Source	136	65	69	270
Time variation[b]	4 (3 %)	10 (15 %)	3 (4 %)	17 (6 %)
2MASS counterpart[b]	62 (45 %)	17 (26 %)	8 (12 %)	87 (32 %)
Covered by SOFI[b]	106 (78 %)	47 (72 %)	49 (71 %)	202 (75 %)
SOFI counterpart[c]	88 (83 %)	25 (53 %)	11 (22 %)	124 (61 %)
NIR counterpart[d]	98 (72 %)	30 (46 %)	14 (20 %)	142 (53 %)

[a]Sources associated with the thermal blob-like feature CXOU J184357-035441 (Ueno et al. 2003).

[b]The percentage gives the fraction among all the point sources, excluding the extended sources. Note that the 2MASS covers the entire *Chandra* field, but SOFI does not.

[c]The percentage gives the fraction among the point sources covered by SOFI.

[d]Presence of either 2MASS or SOFI counterparts. The percentage gives the fraction among all the point sources.

Table 4.   Spectral fitting results of the average spectra with absorbed power-law model

hardness ratio	Soft ≤ -0.60	Medium -0.59 to 0.1	Hard ≥ 0.11
Sources with NIR counterparts			
N_H (10^{22} cm^{-2})	0.50 ± 0.05	0.9 ± 0.1	3.5 ± 0.4
photon-index	$2.8^{+0.2}_{-0.1}$	2.0 ± 0.2	0.90^d
N^a	1.5 ± 0.2	$1.6^{+0.4}_{-0.3}$	1.34 ± 0.11
reduced χ^2 (dof)	1.7 (181)	0.99 (137)	1.2 (62)
observed flux^b (0.5 – 10 keV)	2.1	4.7	17
intrinsic flux^c (0.5 – 10 keV)	4.8	7.8	23
Sources without NIR counterparts			
N_H (10^{22} cm^{-2})	0.50 ± 0.15	1.6 ± 0.5	5.0 ± 0.8
photon-index	2.8^d	2.0^d	$0.9^{+0.1}_{-0.3}$
N^a	0.85 ± 0.2	2.9 ± 0.3	$1.8^{+0.9}_{-0.7}$
reduced χ^2 (dof)	1.7 (29)	1.1 (45)	1.27 (170)
observed flux^b (0.5 – 10 keV)	1.2	7.1	23
intrinsic flux^c (0.5 – 10 keV)	2.7	13	33

[a]Power-law normalization in 10^{-6} photons s^{-1} keV^{-1} cm^{-2} at 1 keV.

[b]Average source flux in units of 10^{-15} ergs s^{-1} cm^{-2}.

[c]Intrinsic source flux in units of 10^{-15} ergs s^{-1} cm^{-2} when hydrogen column density is set to null.

[d]Fixed to the best-fit value obtained for the other group in the same spectral hardness with/without NIR counterpart.

Note. — Errors correspond to 90 % confidence.

Table 5. Spectral fitting results of the average spectra with physical models

	With NIR counterparts	Without NIR counterparts
Soft spectra (two MEKAL model)		
Overall normalization[a]	1.0	0.52
N_H (10^{22} cm^{-2})	1.19 ± 0.15	
kT (keV; soft)	0.25 ± 0.02	
N^b(soft)	56	
kT (keV; hard)	2.2 ± 0.5	
N^b(hard)	2.8	
reduced χ^2 (dof)	1.35 (179)	1.85 (30)
Medium spectra (two MEKAL model)		
N_H (10^{22} cm^{-2})	1.4 ± 0.3	···
kT (keV; soft)	0.23 ± 0.10	···
N^b(soft)	68	···
kT (keV; hard)	3.0 ± 0.4	···
N^b(hard)	5.5	···
reduced χ^2 (dof)	1.21 (89)	···
Hard spectra (power-law with iron line and edge)		
N_H (10^{22} cm^{-2})	4.5 ± 0.3	4.8 ± 0.6
photon-index	1.47 ± 0.03	0.77 ± 0.20
N^c	3.26	1.57
E_{line} (keV)	6.67 ± 0.08	6.71 ± 0.08
Line intrinsic width (keV)	< 0.05	0.18 ± 0.11
Line equivalent width (eV)	540 ± 200	340 ± 270
E_{edge} (keV)	···	7.11 (frozen)
Edge depth	···	1.2 ± 0.5
reduced χ^2 (dof)	1.06 (59)	1.28 (67)

[a]The same two temperature MEKAL model parameters are used for the soft spectra with or without the NIR counterparts with the exception of the overall normalization. Hydrogen density of the plasma is fixed to $n_H = 1$ cm^{-3}. Parameter errors are for the spectrum with NIR counterparts.

[b]MEKAL model normalization, $10^{-20}/4\pi d^2 \int n_e n_H dV$, where d is distance (cm), n_e and n_H are electron and hydrogen densities (in cm^{-3}), respectively.

[c]Power-law normalization in 10^{-6} photons s^{-1} keV^{-1} cm^{-2} at 1 keV.

Note. — Errors correspond to 90 % confidence. The spectral model for the medium sources without NIR counterpart is given in Table 4.

Table 6. Iron line parameters of the Galactic diffuse emission

	Energy (keV)	Line flux (photons s^{-1} cm^{-2} str^{-1})	Equivalent width (eV)	Identification
Single line model[a]				
	$6.52\pm^{0.08}_{0.14}$	0.55 ± 0.39	170 ± 120	NEI plasma?
Three line model[b]				
	6.40 (fixed)	$0.6\pm^{0.3}_{0.6}$	$100\pm^{50}_{100}$	Fluorescence from low-ionized iron
	6.67 (fixed)	$0.4\pm^{0.8}_{0.3}$	$180\pm^{360}_{140}$	He-like iron
	6.97 (fixed)	$0.5\pm^{0.8}_{0.5}$	$160\pm^{260}_{160}$	H-like iron

[a]Reduced $\chi^2 = 0.83$ with dof=4.

[b]Reduced $\chi^2 = 1.19$ with dof=3.

Note. — Errors correspond to 90 % confidence. Intrinsic line width is fixed to zero, assuming that the lines are narrower than the instrumental width (~ 100 eV).

Table 7. Low energy line parameters of the Galactic diffuse emission

Energy (keV)	Line flux (photons/s/cm^2/str)	Equivalent width (eV)	Identification
$1.021\pm^{0.009}_{0.002}$	$0.60\pm^{0.14}_{0.11}$	$64\pm^{15}_{12}$	Ne X,Lyα (1.02 keV)
$1.13\pm^{0.07}_{0.03}$	$0.12\pm^{0.12}_{0.09}$	$13\pm^{13}_{10}$	Fe L?
$1.32\pm^{0.02}_{0.01}$	0.32 ± 0.08	36 ± 10	Mg XI, Kα (1.35 keV)
$1.46\pm^{0.04}_{0.03}$	$0.11\pm^{0.11}_{0.08}$	$12\pm^{12}_{9}$	Mg XII, Lyα (1.47 keV)
$1.74\pm^{0.06}_{0.04}$	<0.32	<25	Low ionized Si?
$1.849\pm^{0.003}_{0.017}$	$0.87\pm^{0.17}_{0.46}$	$110\pm^{20}_{10}$	Si XIII, Kα (1.86 keV)
2.00 (fixed)	$0.05\pm^{0.11}_{0.05}$	$6\pm^{13}_{6}$	Si XIV, Lyα (2.00 keV)
$2.188\pm^{0.012}_{0.034}$	0.48 ± 0.24	60 ± 30	Si XIII, Kβ (2.18 keV)
2.42 ± 0.02	0.71 ± 0.15	90 ± 20	S XV, Kα (2.45 keV)
$2.61\pm^{0.04}_{0.05}$	0.30 ± 0.14	40 ± 20	S XVI, Lyα (2.62 keV)
3.08 ± 0.03	0.34 ± 0.12	48 ± 17	Ar XVII, Kα (3.12 keV)

Note. — Reduced $\chi^2 = 1.03$ with dof = 27. Errors correspond to 90 % confidence. Intrinsic line width is fixed to zero, assuming it is narrower than the instrumental width (~ 100 eV).

Table 8.   Two NEI model fitting of the Galactic diffuse emission

	Fixed abundance model	Free abundance model
Soft Component		
kT (keV)	0.86	0.59 ± 0.09
$\log n_e t$ (cm^{-3} s)	11.1	11.8 ± 0.5
Abundance (except Ne, Mg, Si)	0.11	0.044 ± 0.037
Ne abundance	0.11	0.30 ± 0.2
Mg abundance	0.11	0.14 ± 0.06
Si abundance	0.11	0.25 ± 0.05
N_H (10^{22} cm^{-2})	0.75	0.81 ± 0.12
Observed flux[a] (ergs cm^{-2} s^{-1} str^{-1})	3.1×10^{-8}	2.6×10^{-8}
Intrinsic flux[a] (ergs cm^{-2} s^{-1} str^{-1})	1.0×10^{-7}	1.1×10^{-7}
Hard Component		
kT (keV)	6.52	5.0 ± 0.8
$\log n_e t$ (cm^{-3} s)	10.18	10.6 ± 0.1
Abundance (except Fe)	0.23	0.17 ± 0.04
Fe abundance	0.23	0.9 ± 0.3
N_H (10^{22} cm^{-2})	4.00	3.9 ± 0.4
Observed flux[a] (ergs cm^{-2} s^{-1} str^{-1})	2.1×10^{-7}	2.1×10^{-7}
Intrinsic flux[a] (ergs cm^{-2} s^{-1} str^{-1})	8.1×10^{-7}	7.6×10^{-7}
reduced χ^2 (dof)	1.97 (68)	1.52 (64)

[a]In 0.7 – 10 keV.

Note. — Errors correspond to 90 % confidence.